Molecular outflows in z > 6 unobscured QSO hosts driven by star formation

Butler, K.M.; Werf, P.P. van der; Topkaras, T.; Rybak, M.; Venemans, B.P.; Walter, F.; Decarli, R.

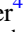# Molecular Outflows in $z > 6$ Unobscured QSO Hosts Driven by Star Formation

Kirsty M. Butler[1,2] , Paul P. van der Werf[2] , Theodoros Topkaras[2], Matus Rybak[2,3] , Bram P. Venemans[2] ,
Fabian Walter[4] , and Roberto Decarli[5]
[1] Institut de Radioastronomie Millimétrique (IRAM), 300 rue de la Piscine, F-38400 Saint-Martin-d'Hères, France; kirstymaybutler@gmail.com
[2] Leiden Observatory, Leiden University, PO Box 9513, 2300 RA Leiden, The Netherlands
[3] THz Sensing Group, Faculty of Electrical Engineering, Mathematics and Computer Science, TU Delft, The Netherlands
[4] Max-Planck Institute for Astronomy, Konigstuhl 17, D-69117 Heidelberg, Germany
[5] INAF—Osservatorio di Astrofisica e Scienza dello Spazio di Bologna, via Gobetti 93/3, I-40129, Bologna, Italy
Received 2022 April 6; revised 2022 December 7; accepted 2022 December 18; published 2023 February 17

Abstract

Feedback and outflows in galaxies that are associated with a quasar phase are expected to be pivotal in quenching the most massive galaxies. However, observations targeting the molecular outflow phase, which dominates both the mass and momentum and removes the immediate fuel for star formation, are limited in high-z QSO hosts. Massive quiescent galaxies found at $z \sim 4$ are predicted to have quenched star formation already by $z \sim 5$ and undergone their most intense growth at $z > 6$. Here, we present two Atacama Large Millimeter/submillimeter Array (ALMA) detections of molecular outflows, traced by blueshifted absorption of the OH 119 μm doublet, from a sample of three $z > 6$ infrared luminous QSO hosts: J2310+1855 and P183+05. OH 119 μm is also detected in emission from P183+05, and tentatively in the third source: P036+03. Using similar assumptions as for high-z dusty star-forming galaxy outflows, we find that our QSOs drive molecular outflows with comparable mass outflow rates, which are comparably energetic except for J2310+1855's significantly lower outflow energy flux. We do not find evidence, nor require additional input from the central active galactic nucleus (AGN) to drive the molecular outflow in J2310+1855, but we cannot rule out an AGN contribution in P183+05 if a significant AGN contribution to L_{FIR} is assumed and/or if the outflow covering fraction is high ($\geqslant 53\%$), which evidence from the literature suggests is unlikely in these sources. Differences observed in the blueshifted absorption spectral properties may instead be caused by the QSO hosts' more compact dust continuums, limiting observations to lower altitude and more central regions of the outflow.

Unified Astronomy Thesaurus concepts: High-redshift galaxies (734); Galactic winds (572); AGN host galaxies (2017); Quasars (1319); Stellar feedback (1602)

1. Introduction

Feedback from star formation and black hole activity plays a critical role in the evolution of galaxies and galaxy populations throughout their lifetimes. Energy and momentum injected back into the interstellar medium (ISM) through these processes regulates galaxy growth by heating, disturbing, or ejecting gas that may have fueled future star formation. The removal of low angular momentum and metal-enriched material from the centers of galaxies via outflows is an essential step in our understanding and ability to reproduce observed disky galaxy morphologies, metallicity gradients, and the polluted circumgalactic (CGM)/intergalactic (IGM) media (Meyer & York 1987; Somerville & Primack 1999; Simcoe et al. 2004; Veilleux et al. 2005; Keres et al. 2009; Governato et al. 2010; Travascio et al. 2020).

Regulated galaxy growth implies that the most rapidly evolving galaxies must also experience the most vigorous feedback. For massive quiescent galaxies observed as early as $z > 4$ (Straatman et al. 2014; Guarnieri et al. 2019; Carnall et al. 2020; Valentino et al. 2020), their short but explosive lifetimes must have been accompanied by extreme star formation and subsequent feedback and outflows, in order to deplete their gas reserves by this time (Glazebrook et al. 2017;

Estrada-Carpenter et al. 2020; Forrest et al. 2020). High-z ($z > 4$) dusty star-forming galaxies (DSFG) that also host an active galactic nucleus (AGN) thus present the most probable progenitors of such systems, warranting an investigation into the scale and impact of their outflows.

At low redshift, observations of the ionized and neutral phases have shown that outflows are ubiquitous (Veilleux et al. 2005; Heckman & Thompson 2017; Rupke 2018; Veilleux et al. 2020). With the advent of Herschel, observations extended to the cooler neutral and molecular phases and revealed that the associated denser gas that is directly associated with star formation dominates the mass and momentum budget of their outflows (Fluetsch et al. 2021). The first such detections uncovered a molecular outflow in Mrk 231 via emission in the high-velocity line wings of the CO molecule (Feruglio et al. 2010) and via absorption in a P-Cygni profile of the OH molecule (Fischer et al. 2010). Outflows have since been detected in various atomic and molecular species (CO, H_2O, HCN, [C II], [C I], OH^+, OH, CH^+, H_2O^+, etc.), using the same techniques. At high-z, however, high-velocity line wings which typically make up only a few percent of the total emission line flux, become difficult to detect and disentangle, making CO an inefficient tracer. Even observations of the bright [C II] line has detected outflows in only a handful of individual galaxies (e.g., Fan et al. 2018; Herrera-Camus et al. 2021; Tripodi et al. 2022), and can depend strongly on the methodology implemented (Maiolino et al. 2012; Cicone et al. 2015; Meyer et al. 2022). Stacking has

helped to provide additional detections (Gallerani et al. 2018; Ginolfi et al. 2020), but not without some contradictory results (Bischetti et al. 2019; Novak et al. 2020). Most convincingly, Spilker et al. (2020a) show in their Section 5.2 that even high-quality [C II] spectra, with comparable or higher signal-to-noise ratios (S/Ns) than the stacked results mentioned, do not show evidence of high-velocity wings in sources with known molecular outflows, thus deeming [C II] as an unreliable outflow tracer of molecular gas.

Absorption lines, on the other hand, have proven to trace the gas intervening the observer and host galaxy in dusty high-z sources efficiently (Falgarone et al. 2017; Indriolo et al. 2018; Spilker et al. 2020a, 2020b; Berta et al. 2021; Butler et al. 2021; Riechers et al. 2021; Shao et al. 2022), reliably detecting inflowing and outflowing gas when redshifted or blueshifted with respect to the host galaxy's systemic velocity.

The OH molecule is the most extensively utilized of such species, with samples in the local universe spanning star-forming, composite, and AGN-dominated systems (Sturm et al. 2011; Spoon et al. 2013; Veilleux et al. 2013; Calderón et al. 2016; Stone et al. 2016; González-Alfonso et al. 2017). Consistently throughout these studies, the outflow properties are found to correlate best with the AGN luminosity L_{AGN} or AGN fraction α_{AGN} of the host galaxy, and at best only weakly with the host galaxy's star-forming properties (Calderón et al. 2016). Higher L_{AGN} and α_{AGN} drive faster outflow velocities (Sturm et al. 2011; Spoon et al. 2013; Stone et al. 2016) and shorter gas-depletion timescales (Sturm et al. 2011; González-Alfonso et al. 2017). The total OH absorption line equilivant widths (EWs) strongly correlate with 9.7 μm silicate absorption, a measure of obscuration within the host galaxy (Stone et al. 2016), while the relative strength of the OH emission component decreases (Spoon et al. 2013; Veilleux et al. 2013). Furthermore, pure OH emission spectra found in some AGN-dominated systems display relatively narrow line widths, suggested to be indicative of a stage after which the AGN has cleared the obscuring material (Veilleux et al. 2013).

At high-z, observations targeting OH are mostly limited to star-forming galaxies (Spilker et al. 2018, 2020a, 2020b), and one tentative absorption detection in the $z = 6.13$ QSO, ULAS J131911+095051 (Herrera-Camus et al. 2020). OH absorption is detected in all of the 11 SPT sources targeted by Spilker et al. (2020a, 2020b), with no sources displaying OH in emission. At a similar rate to low-z ultraluminous infrared galaxies (ULIRGs) and QSOs, 73% display unambiguous evidence of outflows, none of which could be detected by high-velocity wings in their corresponding [C II] spectra. Such a high detection rate indicates a typical outflow geometry that has either a wide opening angle or is widespread. In either case, the outflows display significant clumping unlike the smooth dust continuum profiles of these galaxies. The covering fractions of the clumpy outflows increase with both the galaxy's infrared (IR) luminosity and outflow velocity.

With no evidence and no requirement of AGN feedback needed to drive the molecular outflows studied in the high-z DSFG sample, and with only one tentative detection of OH absorption in a QSO at $z > 6$, there is a clear gap in our understanding of how and if AGN activity contributes to the ejection of molecular outflows in the early universe. In this paper we present molecular gas observations of the 119 μm OH doublet in three luminous $z > 6$ QSOs and their FIR-bright host galaxies: J231038.88+185519.7 (hereafter J2310+1855,

$z = 6.00282$), PSO J183.1124+05.0926 (hereafter P183+05, $z = 6.43862$), and PSO J036.5078+03.0498 (hereafter P036 +03, $z = 6.54052$).

In Section 2 we present the Atacama Large Millimeter/submillimeter Array (ALMA) band 7 observations, reduction, and imaging of the OH 119 μm line and continuum in these sources. In Section 3 we explore the spectral properties of the OH line and relationship to the host galaxy properties, making comparisons to the high-z DSFG sample of Spilker et al. (2020a, 2020b) and low-z sample of Veilleux et al. (2013). In Section 4 we derive outflow properties, consider the driving mechanisms required, as well as the possible impact on the future of the host galaxy. In Section 5 we discuss the the significance of spectral differences found between the QSO and high-z DSFG samples and the context of the observed molecular outflows within the evolution of the host galaxies and QSOs. In Section 6 we summarize our conclusions. Throughout the paper we adopt a flat ΛCDM cosmology with $\Omega_m = 0.307$ and $H_0 = 67.7 \, \mathrm{km \, s^{-1} \, Mpc^{-1}}$ (Ade et al. 2016).

2. Sample, Observations, and Imaging

The data presented in this paper were taken as part of the ALMA Cycle 6 project 2018.1.01790.S (P.I.: P.P. van der Werf) targeting three far-IR-bright QSOs: J2310+1855, first identified in the Sloan Digital Sky Survey (SDSS) (Jiang et al. 2016), and P183+05 and P036+03, both selected as z-dropouts in the PanSTARRS1 survey (Chambers et al. 2016) and first reported by Mazzucchelli et al. (2017) and Venemans et al. (2015), respectively. Bañados et al. (2019) reported the presence of a damped Lyα absorber (DLA) in the proximity zone of P183+05, at $z = 6.40392$. At this redshift the OH 119 μm doublet lies just outside our frequency coverage at 340 GHz, blueshifted by $-1400 \, \mathrm{km \, s^{-1}}$ with respect to the systemic velocity of P183+05's host galaxy. All three sources have previously been studied in resolved FIR and [C II] emission with kinematic modeling (Wang et al. 2013; Bañados et al. 2015; Decarli et al. 2018; Feruglio et al. 2018; Shao et al. 2019; Pensabene et al. 2020; Venemans et al. 2020; Neeleman et al. 2021; Tripodi et al. 2022) and observed in various additional lines (Venemans et al. 2015; Chambers et al. 2016; Jiang et al. 2016; Feruglio et al. 2018; Bañados et al. 2019; Li et al. 2020; Decarli et al. 2022; Shao et al. 2022; Tripodi et al. 2022). A summary of key properties taken from the literature is shown in Table 1.

For each source, the ALMA band 7 receivers were tuned such that two overlapping spectral windows of one side band covered the OH 119 μm line, with the remaining two spectral windows placed to detect the underlying dust continuum at a high S/N. All sources were observed with 43 ALMA antennas, in good conditions. Specific details of the observations and imaging for each source can be found in Table 2.

The raw data were reduced using CASA (McMullin et al. 2007) version 5.4.0–70 for J2310+1855 and CASA version 5.4.0–68 for P183+05 and P036+03. All sources were noninteractively imaged using `tclean` down to a cleaning threshold of 1σ and a robust weighting of 0.5, which was found to optimized the S/N without losing significant spatial resolution. We separate the data into two data cubes for each side band, with no continuum subtraction and leave the frequency resolution equal to the channel resolution of 15.624464 MHz. The rest-frame 119 μm continuum map was created using the available line-free channels in each source.

Table 1
QSO Host Galaxy Properties from the Literature

Name	$z_{[CII]}$	(kpc $''^{-1}$)	$L_{[CII]}$ 10^9 ($L_\odot$)	L_{FIR} 10^{12} ($L_\odot$)	M_{1450} (mag)	M_{gas} 10^{10} ($M_\odot$)	M_{dyn} 10^{10} ($M_\odot$)	i (deg)	v_{rot} (km s^{-1})	v_{rot}/σ_V (km s^{-1})
J2310+1855	6.00282[d]	5.84	8.83 ± 0.44[c]	$15.0^{+0.39}_{-0.33}$[e]	−27.75[d]	4.4 ± 0.2[e]	$5.2^{+2.3}_{-3.2}$[e]	25[e]	≃347[e]	∼6[e]
P183+05	6.43862[b]	5.61	7.15 ± 0.32[b]	10.53 ± 0.36[b]	−26.99[d]	$5.0^{+27.8}_{-2.1}$[a]	$>13.0^{+7.8}_{-9.1}$[a]	<22[a]	>320[a]	2.29[a]
P036+03	6.54052[b]	5.56	3.38 ± 0.09[b]	5.77 ± 0.12[b]	−27.28[d]	$2.8^{+15.4}_{-1.1}$[a]	$2.9^{+1.1}_{-0.7}$[a]	21^{+5}_{-4}[a]	200^{+50}_{-30}[a]	3.21[a]

Note. Properties of the QSOs and host galaxies taken from the literature. To obtain L_{FIR} for J2310 we find the conversion between L_{TIR} and L_{FIR} using the modified blackbody component of the best-fit spectral energy distribution of Tripodi et al. (2022). This gives $L_{TIR}/L_{FIR} = 1.6$. References: (a) Neeleman et al. (2021), (b) Venemans et al. (2020), (c) Wang et al. 2013, (d) Mazzucchelli et al. (2017), and (e) Tripodi et al. (2022).

Table 2
ALMA Observations

		J2310+1855	P183+05	P036+03
R.A.	[hh:mm:ss]	23:10:38.90	12:12:26.98	02:26:01.88
Decl.	[dd:mm:ss]	+18:55:19.82	+05:05:33.49	+03:02:59.39
t_{obs}	[min]	34.50	44.28	39.50
Beam	['']	0.56 × 0.48	0.58 × 0.45	0.63 × 0.44
σ_{cont}	[μJy beam^{-1}]	3.31	0.65	0.99
Δchan	[km s^{-1}]	13.1	13.9	14.1
$\overline{\sigma}_{chan}$	[μJy beam^{-1}]	12.5	4.18	6.48

Note. $\overline{\sigma}_{chan}$ is the mean channel sensitivity, for a channel width of Δchan, in the side band containing the OH 119 μm doublet.

3. Results

3.1. Spectra and Spectral Fitting

The rest-frame 119 μm dust continuum is detected at high S/N and marginally resolved in each of our sources (Figure 2). The integrated spectra shown in Figure 1 are created by stacking all spaxels with a continuum level $>8\sigma$ in the corresponding continuum map. This is done for both side bands. The OH 119 μm doublet is clearly detected in absorption for two sources (J2310+1855 and P183+05), both blueshifted with respect to the systemic velocity of their respective host galaxies. OH 119 μm absorption is not found at systemic velocities in any of the sources. OH 119 μm is also detected in emission at systemic velocity in P183+05, forming a P-Cygni profile in the spectra of this source, and tentatively detected at the systemic velocity in P036+03. This is in contrast with the sample of high-z DSFGs studied by Spilker et al. (2020a), where OH 119 μm emission was not detected in any of the sources. We discuss this result in Section 5.4.

We fit each spectrum across both side bands, with a combination of one or two double Gaussians and an underlying linear dust-continuum slope. The corresponding spectral ranges used are 344.0–360.0 GHz, 335.5–351.0 GHz, and 330.9–346.5 GHz for J2310+1855, P183+05, and P036+03, respectively. The double-Gaussian component consists of two Gaussians of equal amplitude and width, and placed at a fixed rest-frame separation of 4.37 GHz, as required of the OH Λ–doublet at the redshift under consideration. The continuum flux density and slope are left as free parameters as well as the amplitude and width of the double Gaussian. The frequency offset of the absorption features in J2310+1855 and P183+05 is left as a free parameter while the OH emission features in P183+05 and P036+03 are fixed at the systemic velocity of their hosts. The resulting spectral fits are shown in Figure 1 along with the residual spectra. The residuals of J2310+1855

display possible excess absorption at more blueshifted velocities than is captured by the single double-Gaussian fit, possibly indicating an outflow at even higher velocities. This feature lies at the edge of the side band, however, and additional observations extending to higher frequencies are needed to confirm this additional outflow component. The narrow (108 ± 22 km s^{-1}) line width of the tentative OH emission in P036+03 is comparable to that found for the weak water vapor emission of the blended 3_{22}–3_{13} and 5_{23}–4_{32} H_2O transitions (Bañados et al. 2015), which similarly traces warm, dense molecular gas. The best-fit parameter values and uncertainties for each source are presented in Table 3. Line maps, integrated over the FWHM, are shown in Figure 2.

As is commonly done in the literature, we derive additional quantities of the absorption lines from our best-fit parameters in order to compare our work with previous OH studies (Veilleux et al. 2013; Spilker et al. 2020a; Herrera-Camus et al. 2020). These include the FWHM, EW (equal to the optical depth in the optically thin regime), and three definitions of the absorption line velocity: v_{50}, v_{84}, and v_{max}, referring to the velocities above which 50%, 84%, and 98% of the absorption lies, respectively. These values are also found in Table 3 and presented in Figure 3 as functions of the far-infrared (FIR) luminosity and EW.

For comparison, Figure 3 also shows results from previous samples of OH absorption in star-forming and AGN hosts at both low-z (Veilleux et al. 2013; Stone et al. 2016) and high-z (Spilker et al. 2020a; Herrera-Camus et al. 2020). As we are specifically interested in the outflowing molecular gas we additionally plot the outflow-only components of the high-z DSFGs studied by Spilker et al. (2020a) (the separate components are not provided for the low-z sample). The outflow-only components in general show stronger correlations than the full absorption line values. Furthermore, we find that the strongest correlation with outflow velocity is associated with V_{50} and not V_{max}, as is found in studies that use the total (systemic and blueshifted) absorption lines. The tighter relation found with V_{max} for the full absorption line may be due to the increasing fractional contribution of the outflowing gas to the total absorption signature toward more negative velocities of the absorption line. We provide a fit to the outflow-only components of the DSFG sample in each panel of Figure 3 to guide the reader's eye when comparing these values with the OH outflows in J2310+1855 and P183+05. These fits are illustrative only and are not intended to imply true physical trends in all panels.

A notable difference evident between the OH outflows in the DSFGs and those of J2310+1855 and P183+05 is the offset to smaller FWHMs at similar L_{FIR} for the two QSOs. The central outflow velocities (v_{50}) of the two QSOs appear on or near the
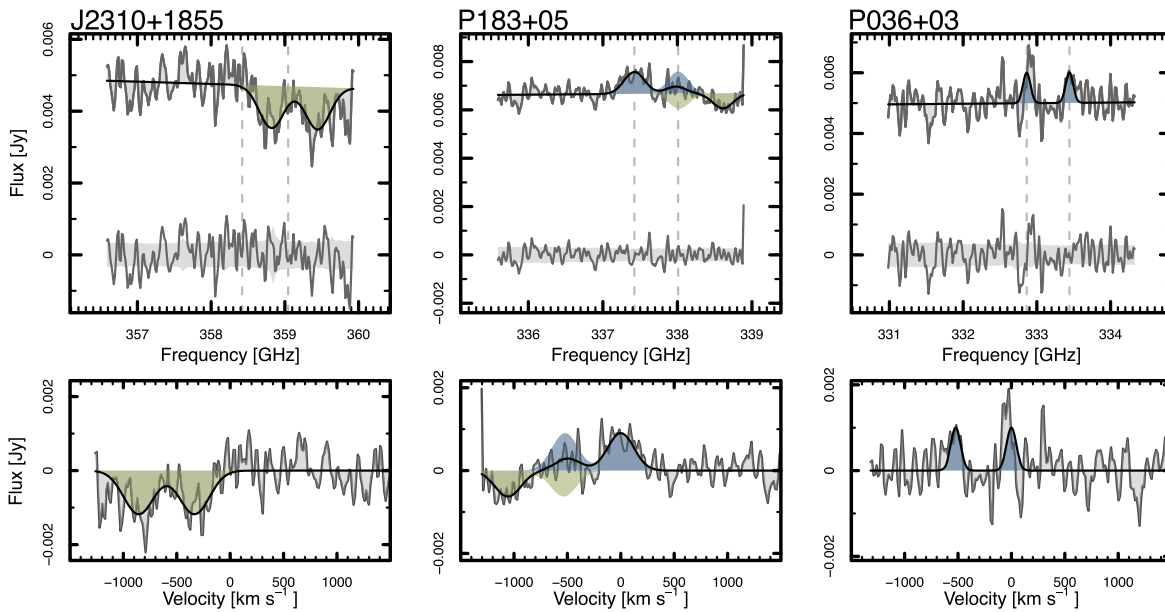
Figure 1. Spectra, with a resolution of 15.6 MHz, of the three QSOs in this paper left to right: J2310+1855, P183+05, and P036+03. Top panels: ALMA spectra of the side band covering the OH 119 μm doublet, as a function of observed frequency with the underling continuum included. The best fit of each spectra are overplotted as a solid black line with individual absorption and emission components shaded in green or blue, respectively. The residuals after subtracting the best fits are shown at the bottom with the channel rms shaded in gray. The rest frequencies of the OH 119 μm doublets, assuming the redshifts in Table 1, are shown by the vertical dashed lines. Bottom panels: the same spectra with the best-fit continuums subtracted, shown as a function of velocity.

DSFG v_{50} versus L_{FIR} trend. The narrower line widths of the QSO lines, however, cause the QSO outflows to drift toward slower than expected velocities for more extreme velocity definitions (v_{84} and $v_{\max}$ versus L_{FIR}). This is also seen in the plots of EW versus V.

A second, notable observation is the large EW of the OH absorption in J2310+1855. Although less extreme in the case of P183+05, the EWs of the OH absorption lines are relatively larger for both J2310+1855 and P183+05 than seen in the DSFGs, given the narrower line widths.

Care should be taken when interpreting the position of ULAS J131911+095051 (Herrera-Camus et al. 2020) in Figure 3 as these values are taken from a single-Gaussian fit. The lower-frequency transition of the OH 119 μm doublet is likely canceled out by emission at systemic velocities, as is seen in P183+05. Some absorption from the higher-frequency transition is also likely lost on the red side of the line, meaning a fit to this absorption feature alone will underestimate the absorption strength and line width and will overestimate the blueshifted velocity offset.

3.2. Source Sizes

For each source we estimate the size of the 119 μm continuum-emitting area. Taking only line-free channels, the visibilities of each data set are binned in radial uv bins. We perform the procedure for bins of uv widths of 10, 25, and 50 $k\lambda$ taking the mean value of the real visibilities in each bin. We perform the fit on the resulting binned data using scipy's `curve_fit` routine, adopting the scatter in the visibilities as the uncertainty. We fit the continuum data with (1) a single Gaussian and (2) a combination of a Gaussian and a point source. A single-Gaussian fit is preferred for all the sources except P183+05. We find mean 119 μm continuum half-light radii of $0\farcs109 \pm 0\farcs009 = 637$ pc, $0\farcs228 \pm 0\farcs008 = 1280$ pc, and $0\farcs127 \pm 0\farcs004 = 707$ pc, for J2310+1855, P183+05, and

P036+03, respectively. The errors include the formal uncertainties from `curve_fit` and the scatter between different uv-binnings. The results are robust with respect to the uv bin size. All sources are marginally resolved by the beam as seen by the distinct drop-off in continuum flux toward larger uv distances in each source (Figure 4).

Our measured half-light radii of J2310+1855 and P183 +05 are comparable to previous high-resolution measurements of the dust continuum at 260 GHz ($R_{1/2} = 0\farcs11 \times 0\farcs095$; Tripodi et al. 2022) and 158 μm ($0\farcs225 \times 0\farcs175$; Venemans et al. 2020), respectively. P036+03's measured half-light radius is large compared to previous high-resolution measurements of $0\farcs095 \times 0\farcs08$ at 158 μm (Venemans et al. 2020). All three QSO sizes are within the range reported for the full 27 QSO hosts studied by Venemans et al. (2020) and the high-z comparison sample of DSFGs (Spilker et al. 2020b).

The same procedure is also applied to continuum-subtracted channels within the FWHM of the lower-frequency line of the OH emission doublet of P183+05, and in both emission components of P036+03 (bottom row of Figure 4). This provides an OH 119 μm emitting radius of $0\farcs63 \pm 0\farcs13 = 3.54$ kpc for P183+05. The OH emission is not resolved in the case of P036+03.

3.3. Outflow Covering Fractions and Detection Rates

A limiting factor of absorption line work is that only gas lying between the observer and the background continuum may be detected. For some geometries, outflowing or inflowing gas may or may not intervene the line of sight (LOS) and background continuum given particular viewing angles. Consequently, a non-detection does not immediately imply the absence of an out/inflow. Likewise, when a detection is made, the observed covering fraction f_{cov} of the intervening gas (the fraction of the background continuum with an absorption signature), may not be indicative of the overall $4\pi f_{\mathrm{cov}}$, unless

Table 3
Measured and Derived Host Galaxy and Outflow Properties

		J2310+1855	P183+05	P036+03
119 μm Contintuum				
$R_{1/2,119\mu m}$	[pc]	637 ± 53	1280 ± 45	707 ± 22
$S_{119\mu m}$	[mJy]	4.73 ± 0.0016	6.66 ± 0.0010	5.00 ± 0.0020
OH 119 μm Emission (systemic)				
$S_{OH\ 119\mu m}$	[Jy km s^{-1}]	...	0.28 ± 0.028	0.12 ± 0.022
$\sigma_{Emis.}$	[km s^{-1}]	...	123 ± 13	45.9 ± 9.5
FWHM$_{Emis}$	[km s^{-1}]	...	289 ± 31	108 ± 22
OH 119 μm Absorption (outflow)				
$S_{OH\ 119\mu m}$	[Jy km s^{-1}]	−0.42 ± 0.04	−0.19 ± 0.03	...
$N_{OH\ 119\mu m}$	[10^{15} cm^{-2}]	8.90 ± 2.1	3.10 ± 0.059	...
EW$_{OF}$	[km s^{-1}]	619 ± 140	215 ± 4.1	...
σ_{OF}	[km s^{-1}]	140 ± 12	123 ± 19	...
FWHM$_{OF}$	[km s^{-1}]	330 ± 29	290 ± 45	...
V_{50}	[km s^{-1}]	−334 ± 14	−534 ± 18	...
V_{84}	[km s^{-1}]	−473 ± 21	−656 ± 79	...
V_{max}	[km s^{-1}]	−622 ± 85	−787 ± 222	...
M_{OF}	[$10^8\ M_\odot$]	25–99	13–140	...
$\dot{M}_{OF}$	[$M_\odot$ yr^{-1}]	1300–5300	560–5900	...
$\dot{p}_{OF}$	[10^{35} dyne]	28–110	19–200	...
$\dot{E}_{OF}$	[10^{43} erg s^{-1}]	4.7–19	5.0–530	...
τ_{OF}	[Myr]	8.3–33	8.4–90	...
τ_{OF+SFR}	[Myr]	4.9–8.8	6.1–18	23

Note. Measured properties of the 119 μm dust continuum (size and flux), OH emission and absorption lines (with formal uncertainties from the fitting procedure), and derived properties of the molecular outflows.
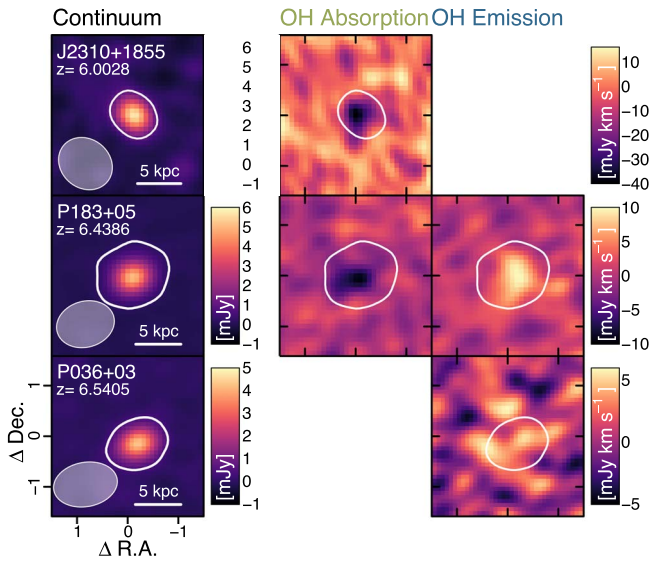

Figure 2. Maps of the three QSOs in this paper top to bottom: J2310+1855, P183+05, and P036+03. From the left: 119 μm continuum intensity maps with the ALMA beam shown as the white ellipse in the lower left corner. This is followed by the OH 119 μm absorption line (J2310+1855 and P183+05) and/or OH 119 μm emission (P183+05 and P036+03) line map. Lines are extracted from channels within the FWHM of the higher- and lower-frequency doublet, for the absorption and emission, respectively. The 8σ continuum level contour is overplotted in white for all maps, indicating the stacking region used to create the spectra shown in Figure 1.

the geometry is known to be isotropic. Assumptions must therefore be made when converting observed column densities to total, galaxy-wide masses (see Section 4).

Measuring the LOS covering fraction requires resolved observations of the intervening gas. Our observations do not resolve the structure of the outflows detected in OH absorption for J2310+1855 and P183+05. We can, however, derive a hard lower bound on the LOS f_{cov} by assuming an optically thick outflow and taking the fractional absorption depth of the OH line. This gives $f_{cov} \geqslant 25\%$ and 9.4% for J2310+1855 and P183+05, respectively, which are comparable to the 5%–20% fractional depths measured by Spilker et al. (2020a) for the high-z DSFGs sample.

The spatial resolution achieved by Spilker et al. (2020a) allowed them to detect distinct clumps in the outflowing OH absorption and measure LOS f_{cov} between 30% and 85% in their lensing reconstructions. They note that these values are upper limits as the individual clumps remain unresolved, accounting for (at least partially) the discrepancy between the LOS f_{cov} and the aforementioned fractional absorption depths. They argue that the true covering fractions are likely closer to those estimated from the peak absorption depth as OH is expected to be highly optically thick. This has similarly been assumed in low-redshift studies (e.g., González-Alfonso et al. 2017).

In any case, f_{cov} measured by Spilker et al. (2020a) is typically smaller than the outflow detection rate of 73% in their sample, interpreted by the authors to imply that the ouflowing gas traced by OH absorption must exit the galaxies in some "fortuitous geometry," one that does not require a special viewing angle. Spilker et al. (2020a) also find positive trends between the covering fraction, FIR luminosity, and outflow velocity, further suggesting that more luminous galaxies,
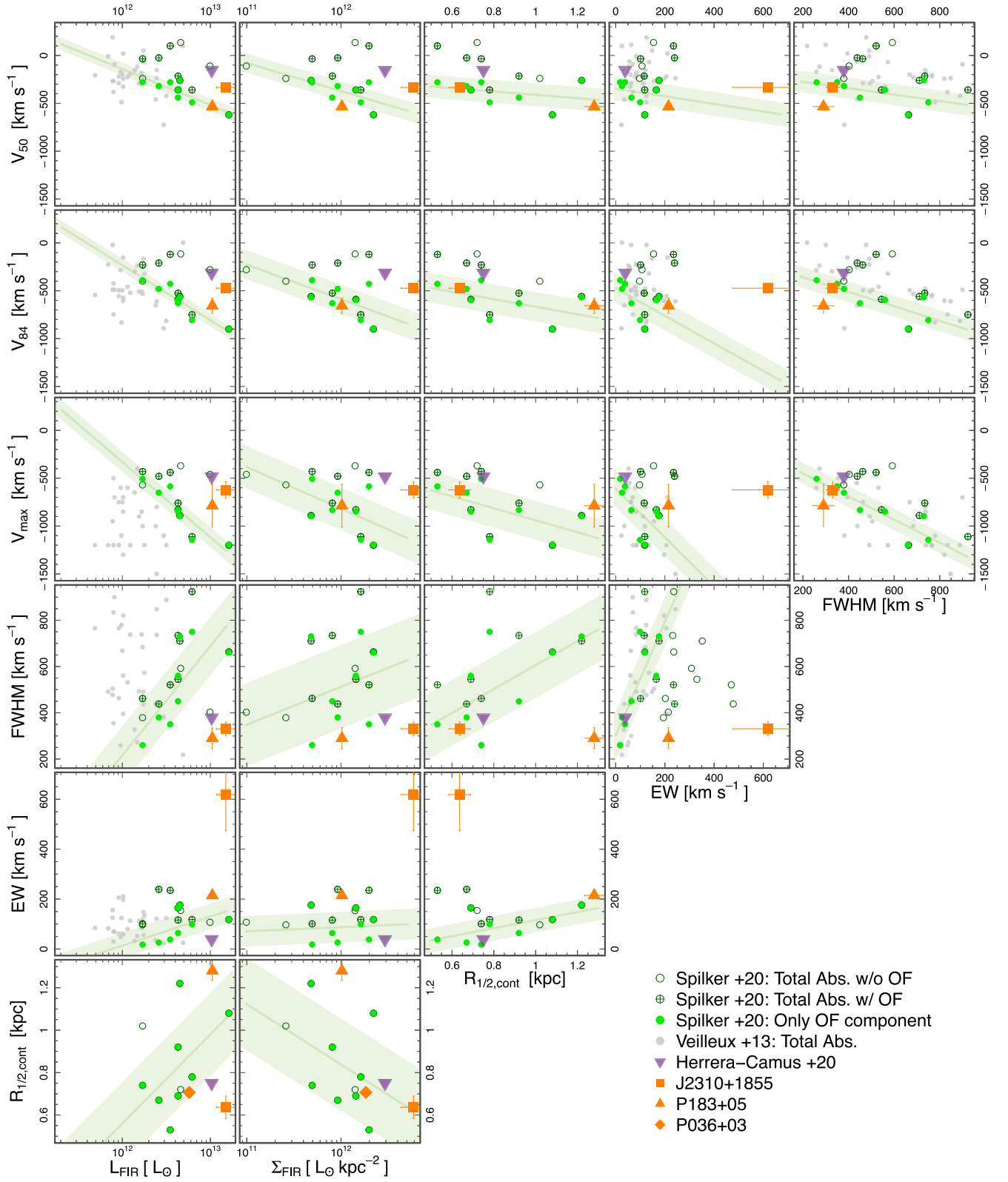
Figure 3. Grid of host galaxy and best-fit OH 119 μm absorption spectra properties. This includes: v_{50}: mean velocity, v_{84}: velocity above which 84% of the absorption lies, v_{max}: velocity above which 98% of the absorption lies, FWHM, EW, L_{FIR}: FIR luminosity of the host galaxy, Σ_{FIR}: FIR surface brightness of the host galaxy given by $L_{FIR}/(2\pi R_{1/2,cont}^2)$, and R_{cont}: effective radius of the 119 μm continuum emission. We show low-z sources in gray, including both star-forming and AGN host galaxies (Veilleux et al. 2013). The spectral properties are measurements of the total (systemic and blueshifted) absorption lines. In green we show the high-z DSFG sample studied by Spilker et al. (2020a, 2020b), further separating this sample into measurements of the total (systemic and blueshifted) absorption line (dark green crossed circles), just the systemic components (dark green open circles), and just the outflowing components (light green filled circles). Sources with only an outflowing component appear as a light green dot with a dark green outline. We display a fit to the outflow-only components in each panel (illustrative only) with a solid line and shade the 1σ scatter, both in light green. We include the tentative OH detection in the $z = 6.13$ QSO, ULAS J131911+095051 (Herrera-Camus et al. 2020; purple triangle). J2310+1855 and P183+05 are shown by the filled orange square and triangle, respectively.
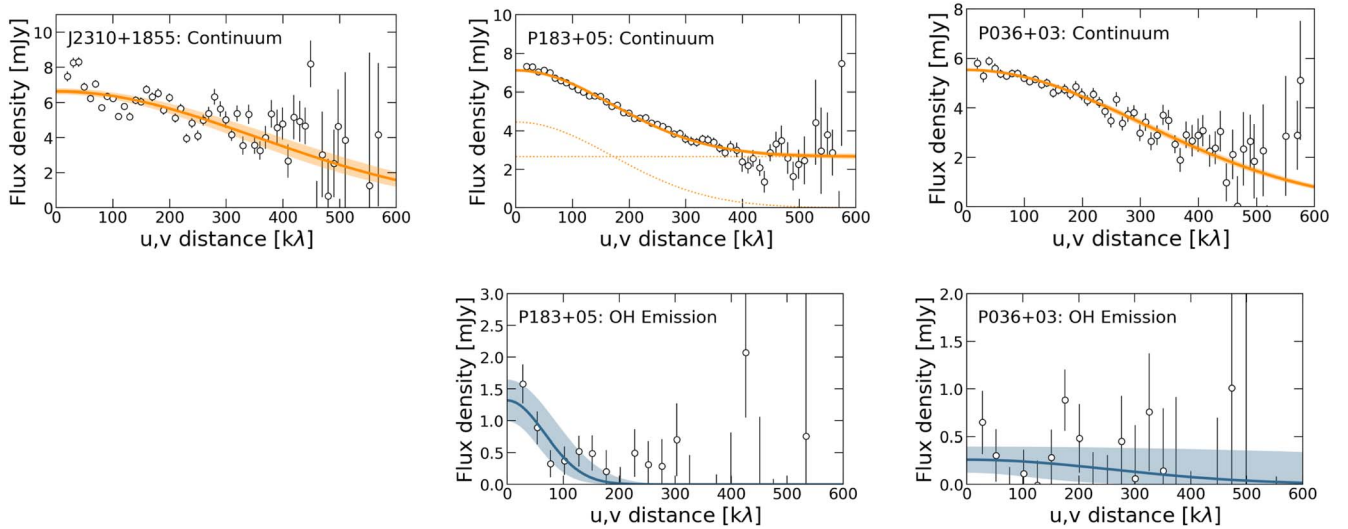
Figure 4. Radial profiles of the dust continuum (top row) and OH 119 μm emission (bottom row) visibilities, using uv bins of width 10 $k\lambda$. The mean values of the real visibilities in each bin are taken from a fit consisting of a Gaussian or a combination of a Gaussian and point-source profile to each source, which we over plot in orange/blue along with with the 1σ uncertainty shaded also in orange/blue. We show the individual components of the combination fit to the continuum of P183+05 with dotted orange curves.

capable of driving more extreme outflows, are either more likely to drive an outflow or drive more widespread outflows (i.e., a wider opening angle/more clumps).

The detection rate of OH outflows in the four currently observed QSOs at $z > 6$ is either 50% or 75%, depending on whether we include the tentative outflow detection of the $z = 6.13$ QSO ULAS J131911+095051 (Herrera-Camus et al. 2020). In the following section we use the fractional absorption depth of the OH line to derive lower limits of the outflow properties. As we cannot measure an upper limit of the covering fraction as Spilker et al. (2020a) did with their high spatial resolution data, we simply use an upper limit of $f_{\rm cov}$ of 100%. We caution the reader when interpreting these upper limits, as a 100% covering fraction is likely unphysical, given the evidence from the literature that OH traces optically thick, widespread and clumpy outflows, thus resulting in covering fractions more comparable with that of the fractional absorption depth.

4. Derived Outflow Properties

In this section we derive the physical and energetic properties of the molecular outflows observed for J2310 +1855 and P183+05. To compare our outflows with those found in the sample of high-z DSFGs studied by Spilker et al. (2020a, 2020b), we recalculate the outflow properties for this sample using the same methods and assumptions adopted for J2310+1855 and P183+05. We consider only the blueshifted outflowing Gaussian component of the OH absorption spectra of the DSFGs when deriving properties of the outflow and do not include the systemic gas component. This differs from the approach of Spilker et al. (2020b), where the outflowing component was defined as absorption seen at velocities < -200 km s^{-1} in the total (systemic and outflowing) absorption line.

4.1. Outflow Mass, Mass Outflow Rate, and Depletion Time

In the optically thin regime, the EW of an absorption line is equal to the integrated optical depth. In this scenario, the EW

can directly replace the optical depth integrated over the velocity, $\int \tau_\nu dv$, when deriving the column density of the OH119 μm, given by,

$$N_{\rm OH} = \int \tau_\nu dv \frac{\nu^3 g_1 8\pi}{c^3 A_{\rm ul} g_{\rm u}}, \qquad (1)$$

where ν is the rest frequency of the line, $g_u = 6$ and $g_1 = 4$ are the upper and lower statistical weights, respectively, and $A_{\rm ul} = 10^{-0.86618}$ s^{-1} is the Einstein coefficient of the transition. $N_{\rm OH}$ is then converted to a total molecular hydrogen column density assuming a conversion factor; here we assume a $N_{\rm OH}/N_{\rm H_2} = 1 \times 10^{-7}$ from Nguyen et al. (2018).

To convert a column density to a full outflow mass and mass outflow rate, the geometry of the outflow must first be assumed. Our marginally resolved observations do not allow the geometry of the outflows observed for J2310+1855 and P183+05 to be determined. We therefore assume a simple spherical thin shell outflow geometry, commonly used elsewhere in the literature (e.g., Rupke et al. 2005), which provides a conservative estimate of the mass and mass outflow rate,

$$\dot{M}_{\rm OF} = 4\pi R_{\rm OF}^2 \mu m_{\rm H_2} f_{\rm cov} N_{\rm H_2} \frac{V_{\rm OF}}{R_{\rm OF}} = \frac{M_{\rm OF} V_{\rm OF}}{R_{\rm OF}}, \qquad (2)$$

where $\mu = 1.36$ accounts for the universal helium fraction, R is the outflow radius, assumed to be $R_{\rm cont}$, $V_{\rm OF}$ is the outflow velocity V_{50}, and $f_{\rm cov}$ is the covering fraction of the outflowing gas.

As discussed in Section 3.3, we cannot measure $f_{\rm cov}$ with our spatially unresolved data. Thus, for the purpose of simply comparing our two QSOs and with the sample of DSFGs, we derive all values of $\dot{M}_{\rm OF}$ using $f_{\rm cov} = 1$, providing upper limits on $M_{\rm OF}$ and $\dot{M}_{\rm OF}$ for the given geometry. For J2310+1855 this gives $M_{\rm OF} < 99 \times 10^8 M_\odot$ and $\dot{M}_{\rm OF} < 5300 M_\odot$ yr^{-1} and for P183+05 $M_{\rm OF} < 140 \times 10^8 M_\odot$ and $\dot{M}_{\rm OF} < 5900 M_\odot$ yr^{-1}.

Figure 5 presents the derived values of $\dot{M}_{\rm OF}$ as a function of FIR luminosity and derived SFR. As previously reported by Spilker et al. (2020b), DSFGs with larger $L_{\rm FIR}$ drive outflows with higher $\dot{M}_{\rm OF}$. Focusing on the upper-limit relations, we find
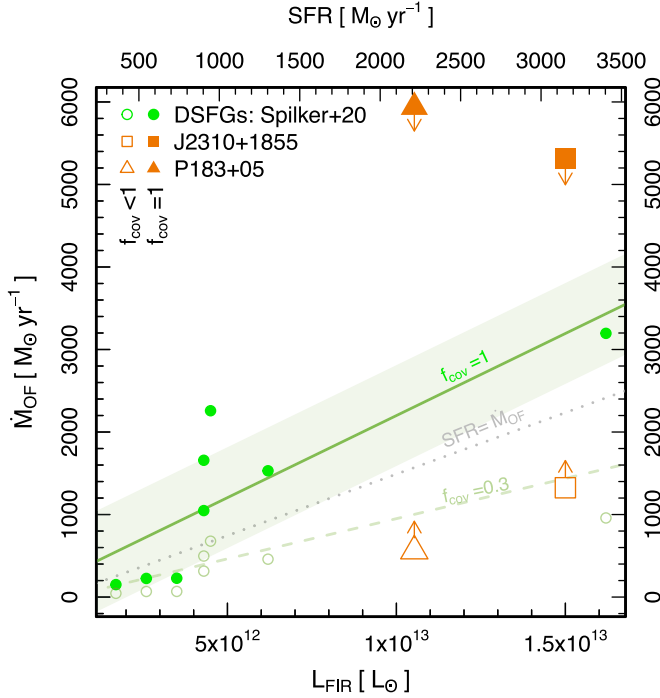
Figure 5. Mass outflow rate as a function of FIR luminosity (bottom axis) and SFR (top axis), assuming a spherical thin shell geometry for all sources. We show the DSFGs (Spilker et al. 2020a, 2020b) in green assuming a covering fraction of 1 (filled) as upper limits and 0.3 (hollow) based on the average covering fractions measured for low-z star-forming galaxies (González-Alfonso et al. 2017). We show a fit to the $f_{cov} = 1$ points with the solid green line and its 1σ spread with a shaded green region. A fit to the $f_{cov} = 0.3$ points is shown by the dashed green line. We indicate J2310+1855 and P183+05 with an orange square and triangle, assuming a covering fraction of 1 (filled) as upper limits and at the level of their fractional OH absorption depths, 25% and 9.4% (hollow), respectively. The SFR = $\dot{M}_{OF}$ line is shown by the gray dotted line.

that J2310+1855 and P183+05 both sit above the DSFG relation. We note however that there is only one DSFG in the L_{FIR} range of the two QSO hosts, and therefore we do not view the QSO offsets to higher $\dot{M}_{OF}$ as significant. In fact if the highest L_{FIR} DSFG is removed then a fit to the remaining DSFGs will extrapolate between the two QSOs. With the assumed geometry and a $f_{cov} = 1$, we derive $\dot{M}_{OF}$s greater than the SFRs of both QSOs, giving lower limits on the gas-depletion time of $\tau_{OF} > 8.3$ Myr and $\tau_{OF} > 8.4$ Myr for J2310+1855 and P183+05, respectively. If star formation is included and assumed to remain constant, the combined depletion times reduce to $\tau_{OF+SFR} > 4.9$ Myr and $\tau_{OF+SFR} > 6.1$ Myr for J2310+1855 and P183+05, respectively.

González-Alfonso et al. (2017) found an average f_{cov} for OH absorption in their low-z star-forming galaxies of 0.3, which if adopted here would shift all but one of the DSFG and both QSO $\dot{M}_{OF}$s below the $\dot{M}_{OF}$ = SFR line. Whether $f_{cov} = 0.3$ is a suitable covering fraction for high-z galaxies and moreover high-z QSOs, is still yet to be shown. As mentioned in Section 3.3, however, the fractional absorption depths of the OH absorption lines provides a hard lower limit of f_{cov}, which in turn can be used to derive a lower limit of M_{OF} and $\dot{M}_{OF}$. This gives $M_{OF} > 25 \times 10^8 M_\odot$ and $\dot{M}_{OF} > 1300 M_\odot$ yr^{-1} for J2310+1855 and $M_{OF} > 13 \times 10^8 M_\odot$ and $\dot{M}_{OF} > 560 M_\odot$ yr^{-1} for P183+05 This corresponds to outflow depletion timescales of $\tau_{OF} < 33$ Myr and $\tau_{OF} < 90$ Myr and combined

timescales of $\tau_{OF+SFR} < 8.8$ Myr and $\tau_{OF+SFR} < 18$ Myr for J2310+1855 and P183+05, respectively.

4.2. Outflow Energetics

The energy $\dot{E}_{OF}$ and momentum $\dot{p}_{OF}$ flux of an outflow can provide insight into the mechanisms needed to drive it. We derive both these values, for J2310+1855, P183+05, and the DSFGs with the same size and geometrical assumptions used to derive $\dot{M}_{OF}$, giving,

$$\dot{E}_{OF} = \frac{1}{2}\dot{M}_{OF}V_{OF}^2, \quad (3)$$

$$\dot{p}_{OF} = \dot{M}_{OF}V_{OF}. \quad (4)$$

As in the last section, we derive these values assuming a covering fraction of 1 for all objects to compare between the DSFGs and the QSOs and again with $f_{cov} = 0.3$, for the DSFGs, and with the fractional absorption depths of the two QSOs as lower limits (Figure 6). This gives limits of the energy fluxes of 4.7×10^{43} erg s^{-1} < $\dot{E}_{OF}$ < 19×10^{43} erg s^{-1} and 5.0×10^{44} erg s^{-1} < $\dot{E}_{OF}$ < 530×10^{44} erg s^{-1}, and of the momentum fluxes of 28×10^{36} dyne < $\dot{p}_{OF}$ < 110×10^{36} dyne and 19×10^{36} dyne < $\dot{p}_{OF}$ < 200×10^{36} dyne, for J2310+1855 and P183+05, respectively.

Again focusing on the upper limit relations: the DSFG sample displays a clear positive trend for both fluxes with L_{IR}. The QSOs sit below and above these relations for J2310 +1855 and P183+05, respectively. J2310+1855's deviation below the L_{FIR}-$\dot{E}_{OF}$ relation, however, is particularly significant. For all sources, the energy and momentum injected by star formation is sufficient to drive the observed outflow, even at the upper limit values. This is perhaps surprising for J2310+1855 and P183+05, where feedback from both star formation and the central AGN is available and may have been expected to collectively drive a stronger outflow than star formation alone. In Section 5 we discuss possible explanations for why we do not see evidence of an AGN contribution and instead see the opposite in the case of J2310+1855.

4.3. Escape Fractions

Not all material ejected via an outflow will escape the host galaxy or the dark matter halo's gravitational potential. Instead some fraction of the material will remain bound to the galaxy and may re-accrete via a galactic fountain at a later time, unless further heating or acceleration is experienced. Some fraction of the outflow, however, may be sufficiently accelerated to pollute the CGM or even IGM, removing mass, momentum, and metals from the galaxy altogether. Below we attempt to estimate a possible escape fraction of the molecular outflow in our two QSOs.

Assuming that the outflow is at a radius of R_{cont} and that the outflow will not be decelerated by swept-up material, or accelerated by radiation pressure, the dynamical masses (Table 1) are enough to retain effectively all of the outflowing molecular gas in both J2310+1855 and P183+05.

5. Discussion

We begin our discussion by first summarizing the known properties of the high-z DSFG sample and their molecular outflows (Spilker et al. 2020a, 2020b). The spatial resolution of
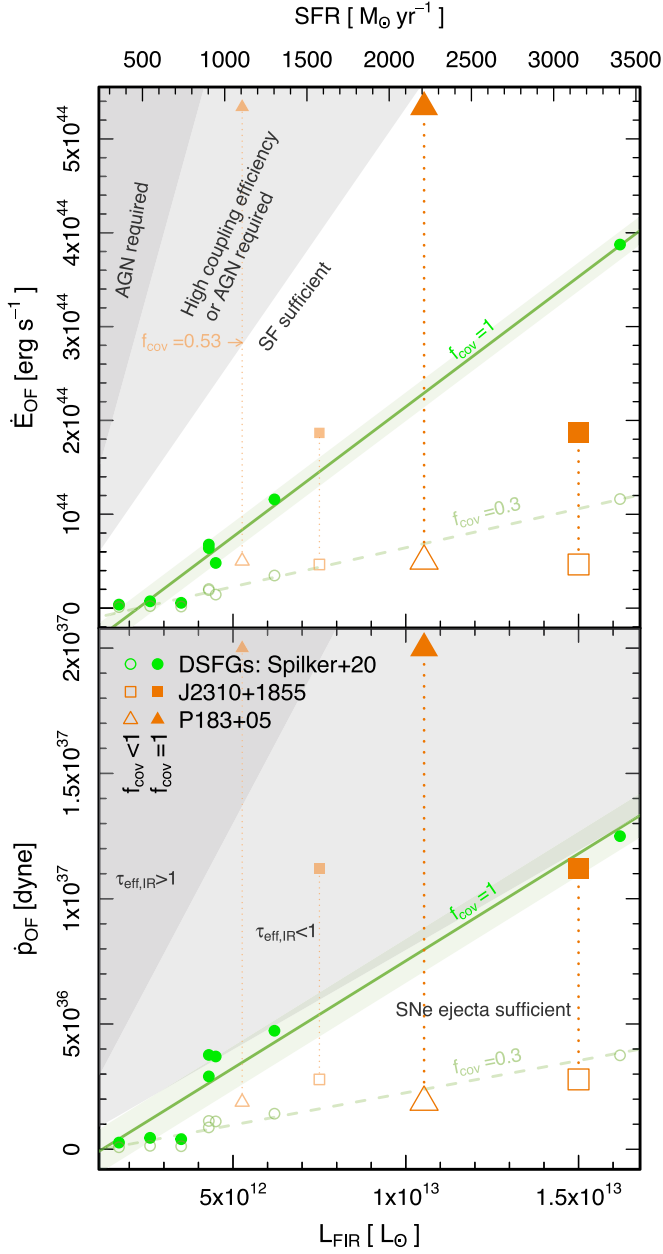
Figure 6. Energy (top) and momentum (bottom) flux as a function of L_{FIR} (bottom axis) and SFR (top axis) derived for the comparison sample of high-z DSFGs (Spilker et al. 2020a, 2020b) (green) and J2310+1855 and P183+05 (orange squares and triangles, respectively). The filled symbols indicate upper limits, assuming an outflow covering fraction of 1. The hollow symbols indicate lower limits for J2310+1855 and P183+05, assuming a covering fraction equal to the fractional OH absorption depth (25% and 9.4%, respectively), and values derived assuming an average covering fraction of 0.3 (González-Alfonso et al. 2017), for the DSFG sample. The smaller faint orange symbols indicate the ranges for J2310+1855 and P183+05 assuming a 50% AGN contribution to L_{FIR} (see the main text). We indicate regions in the top panel where the energy injected via star formation, assuming a maximum coupling fraction to the ISM of 40% (Sharma et al. 2014; Fielding et al. 2018), is equal to the energy flux of the outflow (white), where an unusually high coupling fraction or AGN contribution is required (light gray), and where an AGN is definitely required (darker gray). We indicate regions in the bottom panel where supernova ejecta provide sufficient momentum (white) and where radiation pressure on dust grains in an optically thin (light gray) or thick (darker gray) outflow is needed.

their observations were capable of resolving several distinct clumps in the blueshifted OH absorption, in contrast to the generally smooth background dust continuum. Although not capable of resolving the clumps themselves, Spilker et al. (2020a) use optical depth arguments to predict a substantially more clumpy structure on scales of ∼50–200 pc. The comparatively high detection rate of molecular outflows in the sample compared with the measured covering fractions suggest a fortuitous geometry of the outflows, such that at least a fraction of the outflow is likely to intervene the LOS and background continuum, regardless of the viewing angle. Moreover, higher outflow covering fractions and higher detection rates are found in sources with higher L_{IR}, suggesting that more IR-luminous galaxies are capable of driving either more widespread outflows, outflows with larger opening angles, or larger clump sizes. All three scenarios are consistent with the observed increase in FWHM and EW of the outflowing absorption signature toward higher L_{IR} (Figure 3). Lastly, they find that the optical depths of the outflowing clumps often peak toward the outskirts of the background continuum, offset from the peak in continuum emission. Whether this is the result of a clumpy expanding shell or the removal of more easily ejected gas at lower column densities found at larger radii, remains unclear.

5.1. What Drives Molecular Outflows in Unobscured QSO Hosts?

When treated under the same assumptions, the OH molecular outflows observed for+1855 and P183+05 are less or comparably energetic to those driven by the high-z DSFGs (Figure 6). This is despite harboring comparable SFRs and an additional luminous AGN.

Returning to Figure 3, we highlight the key difference in the basic host galaxy and blueshifted absorption properties between the QSOs and the DSFG sample. First, both QSOs display narrower than expected absorption signatures for their L_{IR} when compared to the DSFG sample. This may be due to a more cohesive outflow velocity structure (i.e., sheet), fewer velocity components contributing to the overall absorption signature (fewer clumps), or an overall less turbulent outflow. P183+05 consistently deviates toward narrower FWHMs from all of the DSFG relations, but does not significantly deviate in any other way with regards to both outflow and host galaxy properties. J2310+1855, on the other hand, deviates in three additional ways: (1) toward much higher outflow absorption strengths (EW), (2) toward slower outflow velocities, and (3) toward a smaller dust continuum size, giving J2310+1855 the highest FIR surface brightness of both samples. We investigate the possible effects of the dust continuum size in Section 5.3.

Our upper limits on the outflow $\dot{M}_{OF}$ and energetics, assuming a covering fraction of 100% around J2310+1855 and P183+05, provide values within the range where the star formation in these systems is sufficient. Not only is additional energy or momentum from an AGN simply not required to drive these outflows, but the fact that J2310+1855 and P183+05's do not even appear to be boosted with respect to the DSFGs in energetics, $\dot{M}_{OF}$, or velocity, suggests that these outflows may indeed be driven by the same mechanisms—those associated with star formation.

5.2. Interaction between Central AGNs and the Surrounding ISM

At low-z, it is consistently found that higher AGN fractions and luminosities drive faster and more energetic molecular

outflows (Sturm et al. 2011; Spoon et al. 2013; González-Alfonso et al. 2017). Outflow properties also correlate best with AGN luminosity or AGN fraction, while only weakly correlating with the star-forming properties of the host galaxy (Calderón et al. 2016). Studies measuring 9.7 μm silicate absorption, which indicates the degree of obscuration originating in a nuclear torus and/or host galaxy disk, find strong correlations with the strength of the OH absorption (EW) (Spoon et al. 2013; Veilleux et al. 2013; Stone et al. 2016). Together, these results suggest that not only the strength of the radiation field, be it from star formation or an AGN, but the obscuration and thus ability of these energy and momentum sources to couple with the surrounding ISM, is crucial in driving a strong molecular outflow. Indeed González-Alfonso et al. (2017) find in their sample of 14 local ULIRGs, that the highest molecular outflow velocities traced by OH absorption are found in buried sources, where slower but more massive expansion of the nuclear gas is found.

But how comparable are low-z AGN hosts compared with our high-z unobscured QSOs? The entire sample studied by González-Alfonso et al. (2017) were galaxies undergoing gas-rich mergers, and indeed AGNs found in the low-z universe are ubiquitously inbedded in such host galaxies (Sanders & Mirabel 1996), where AGN feedback is thought to be stochastically injected into the chaotic surrounding ISM throughout the merging process (González-Alfonso et al. 2017). The three $z > 6$ QSOs studied in this paper, however, all display signatures of orderly, rotationally dominated gas reservoirs (Table 1; Neeleman et al. 2021; Tripodi et al. 2022), opposing a merger scenario. As unobscured QSOs, they have already removed the obscuring material surrounding the AGN, clearing a path through the ISM along the LOS (note: this need not be aligned with the host galaxy).

At high-z, the interaction between central AGNs and their host galaxies is a matter under investigation. Rojas-Ruiz et al. (2021) found that strong synchrotron emission extending into millimeter wavelengths for the radio-loud QSO PSO J352.4034-15.3373 contributed significantly to its FIR luminosity. This source, however is one of the brightest radio-loud sources in the early universe and the subsequent study of Khusanova et al. (2022), considering five radio-loud $z > 6$ QSOs, found that the SFR distribution and [C II] luminosities of their sources were comparable with the radio-quiet population, suggesting that radio jets do not contribute significantly to these properties.

Significant AGN contributions to the FIR luminosity via dust heating have been measured in some high-z QSOs. Schneider et al. (2015) found an AGN contribution between 30% and 70% for the $z = 6.4$ QSO J1148+5251. Although chosen as a prototype for the general population of high-z QSOs, this source harbors an X-ray luminosity twice that of J2310+1855 and has been detected in CO(17-16) (Gallerani et al. 2014) which remains undetected for J2310+1855. Carniani et al. (2019) inspected the CO spectral line energy distributions (SLEDs) and FIR properties of these sources and concluded that the differences found were likely due to different gas heating mechanisms present, those being mechanisms associated with the central AGN for J1148+5251 and star formation for J2310+1855. Decarli et al. (2022) similarly find, using multiline diagnostics and the non-detection of high-J CO transitions, that star formation also appears to drive the molecular gas excitation in P183+05. Duras et al. (2017) found

an average AGN contribution of 50% in their sample of 16 IR-bright QSOs. This sample was chosen to represent an intermediate population of QSOs emerging from the heavily obscured phase, but preceding the blue QSO phase where intervening material has already been swept away. This again differs from the population of unobscured, UV- and FIR-bright QSOs represented by our QSOs.

In a luminosity-limited sample of $z > 6$ unobscured QSOs (including our sources), no correlation is seen between quasar UV luminosity (M_{1450}, see Table 1) and FIR luminosity (Venemans et al. 2018). This is true even in the central regions surrounding the QSOs (Venemans et al. 2020), suggesting little interaction between the QSOs and host galaxy ISM. Our assumption that the SFR dominates the L_{FIR} of our sources is thus likely a good assumption and it is perhaps also unsurprising that we do not find evidence of a boost in the molecular outflow properties measured and derived for our unobscured QSO hosts, compared to the DSFG sample.

In any case, we cannot rule out a contribution from an AGN to the FIR luminosity with this information alone, nor can we ignore the large uncertainties associated with estimating this value (Venemans et al. 2018, 2020; Tripodi et al. 2022). Therefore, as an extreme case, we consider an AGN contribution of 50% to the L_{FIR}, as found for high-z broad absorption line (BAL) QSOs (Duras et al. 2017). We expect, for the reasons stated above, that this value is an upper limit of the AGN contribution for our unobscured sources. This effect would move our sources left, by half, in Figures 5 and 6 and in the left two columns of Figure 3, if one is to consider only the input from star formation. In Figure 3 (note log scales), this makes little difference to our conclusions. In Figures 5 and 6, P183+05 indeed begins to appear more energetic than expected for its SFR, if it is assumed that all the sources have an outflow covering fraction of 100%. This moves the upper limit of the energy flux within the "high coupling efficiency or AGN required" region (indicated by the smaller faint orange symbols). We remind the reader that a covering fraction of 100% is an extreme scenario, with the true values expected to be close to the fractional absorption depth, which in the case of P183+05 is only 9.5%. Assuming an AGN contribution to the FIR of 50%, a high coupling efficiency or an AGN contribution to drive the molecular outflow seen in P183+05 is not required unless the outflow covering fraction is $\geqslant 53\%$. This is higher than all of the absorption depths measured by Spilker et al. (2020a) for the outflowing or systemic gas in their sample. Thus, while it is possible the molecular outflow in P183+05 lies in the parameter space requiring either a high coupling fraction or an AGN contribution, this would require either a significant AGN contribution to the FIR luminosity and/or a high outflow covering fraction ($\geqslant 53\%$). For reasons stated above we believe both the condition of a significant L_{FIR} AGN contribution and/or high covering fraction to move P183+05 into this parameter space to be unlikely, but do not rule it out. For our other source, J2310+1855, a L_{FIR} 50% AGN contribution does not display higher than expected values and does not require a high coupling efficiency or AGN contribution even with a 100% outflow covering fraction. In summary, an AGN contribution to the driving of the molecular outflow in J2310+1855 is not required and is only possibly required for P183+05 under particular extreme scenarios.

Recent results studying the ionized gas phase, however, have found extremely fast outflows up to 17% the speed of light in

$z \sim 6$ QSOs using C IV absorption (Bischetti et al. 2022). Such outflows must transport enormous amounts of energy into the GCM and IGM from the central engine. Included in this sample is J2310+1855, with a detected ionized gas outflow traveling between 18,500 and 27,000 km s^{-1}. Although clearly not associated with the molecular outflowing gas traveling at just ~ 300 km s^{-1}, this may suggest a scenario where a combination of star-formation-driven molecular outflows and AGN-driven ionized outflows work in conjunction to quench these massive active galaxies and transfer energy to the atomic outflows found at higher radii in the surrounding halos of diffuse turbulent gas (as found for J2310+1855 in OH$^+$; Shao et al. 2022). As seen in low-z studies, molecular gas outflows dominate the mass and momentum transport of matter out of the galaxy, while the warmer ionized phases dominate the kinetic energy budget (Fluetsch et al. 2021). The molecular outflows presented here are indeed capable of transporting large amounts of gas, providing short depletion times on the order of megayears predicted for these galaxies (Simpson et al. 2012; Costa et al. 2018). As discussed in Section 4.3, however, a negligible fraction of the outflowing molecular gas will escape the gravitational bind of their host galaxy, and will be re-accreted unless additional energetic input is provided at higher radii. Thus, while the molecular phase may predominantly remove the fuel for future star formation directly from the galaxy, the ionized phase may be responsible for keeping that material at higher radii by efficiently injecting energy into the CGM and thus providing a scenario where these massive gas-rich galaxies can quench on short timescales.

During the QSOs' embedded or blowout phase, however, trapped radiation from the central engine may play a much greater role in launching molecular outflows (Costa et al. 2018). Observing QSOs in these early stages will therefore be crucial in our studies determining the full impact of QSOs on their surrounding ISMs and the role they play in ejecting gas from the galaxy.

5.3. The Background Dust Continuum and its Effect on the Outflow Absorption Signature

The conclusion of the previous subsection does not, however, explain the differences in spectral properties of the OH outflows observed between our $z > 6$ QSO and the high-z DSFGs. The combination of narrower line widths and comparable or higher EWs of the total outflow absorption may imply an increase in the outflow covering fraction or clump positions that preferentially block brighter regions of the background dust emission. Both scenarios may be true in the case of J2310+1855 whose small 119 μm dust size and high surface brightness (Figure 3) means any clumps intervening the LOS will have the tendency to cover brighter regions, and will block a larger fraction of the overall surface area. For galaxy disks at higher inclinations along the observer's LOS, such effects of intervening clouds are further intensified.

We illustrate this effect in Figure 7, for two galaxies of equal luminosity but different sizes (different surface brightnesses), observed at four different inclinations. We consider the effect of the background continuum size and inclination on the observability of foreground clumps traveling in a galactic fountain trajectory, ejected from the center of the galaxy. We show this trajectory for five radial directions but note that clumps may be ejected from anywhere in the galactic plane and travel outwards in any direction. Clumps that intervene the
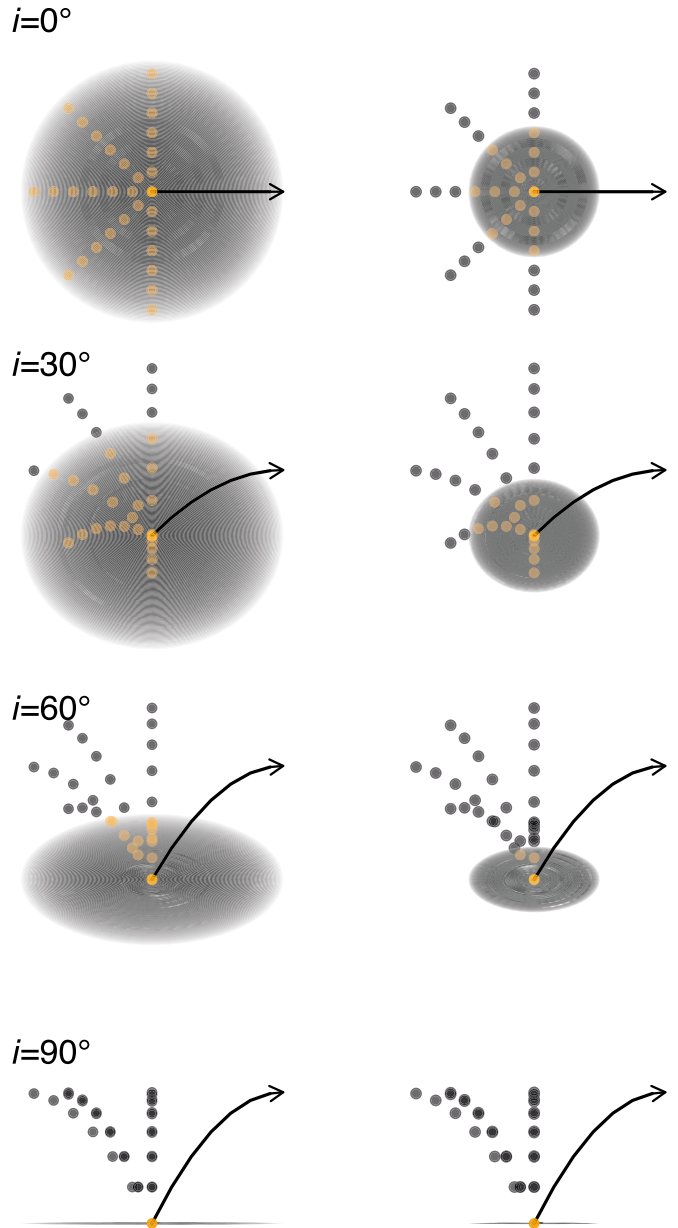

Figure 7. Idealized schematic of two equally luminous disky galaxies (left and right) seen at four different inclinations (from the top: 0°, 30°, 60°, and 90°). We consider a clumpy outflow ejected from the center of the galaxy, traveling radially in five angles covering the left-hand side of the disk, and vertically through a galactic fountain trajectory. On the right we show this trajectory as a solid black arrow. The orange circles indicate clumps that intervene the observer's LOS and the background continuum, and thus contribute to the absorption signature of the outflow. The gray circles indicate when the clumps do not intervene and are invisible to the observer via absorption.

observer's LOS and background dust continuum and are therefore observable via absorption are colored orange. We find that for smaller disk sizes and higher inclinations, absorption line observations become limited to clumps at low radial distances or those lying more toward the foreground. Individual clumps in these circumstances cover a greater fraction of the background dust area and tend to block regions of higher surface brightness, thus imprinting a stronger absorption signature on the global spectrum. Fewer clumps are therefore needed to absorb the same or more background emission, limiting the number of velocity components contributing to the velocity dispersion of the global absorption line.

Without resolving the molecular outflow we cannot say for certain what the geometry or trajectory of the outflowing gas are. Figure 7 does, however, illustrate that clumps at smaller scale heights are preferentially observed. If a clump is initially ejected perpendicular to the disk (the center or farther out), and then continues along a trajectory that deviates from this initial direction, (such as the fountain scenario depicted in Figure 7), the restriction of our observations to low-altitude clumps also restricts our observations to clumps with higher perpendicular velocities. The combined outflow velocity therefore becomes more dependent on the inclination of the disk.

Thus, the smaller disk size of J2310+1855 may cause the absorption signature to be more sensitive to projection effects, contributing to the offset in outflow velocity shown in the first panel of Figure 3. Neither J2310+1855 nor P183+05, however, are found to have significantly inclined disks (25° and <22°), and so it is not expected that projection effects play a dominating role in the slower than expected outflow velocities. We note, however, that Tripodi et al. (2022) found similar results for their dynamical models of J2310+1855 for inclinations over the range of [20, 45]°, and earlier dynamical modeling by Feruglio et al. (2018) using lower-resolution data have previously found a higher inclination of 53°. Tripodi et al. (2022) discarded models with $i > 30°$ due to the gas mass exceeding the dynamical mass, however, this cut off is dependent on the reliability and suitability of the CO conversion factor for a high-z unobscured QSO. In the case of P183+05, which does not display an unusually small continuum size and has only an upper limit on the host galaxy inclination, it is unclear what causes the smaller than expected FWHM of the absorption line and we do not rule out simple natural variance.

Small QSO host dust sizes have been measured for a number of samples at high-z (Ikarashi et al. 2015; D'Amato et al. 2020; Venemans et al. 2020; Stacey et al. 2021), although evidence for an additional shallower extended component is found in the stacking of 27 $z \geqslant 6$ QSO hosts (Novak et al. 2020). Stacey et al. (2021) divided their $z = 1.5$–2.8 QSO hosts into two categories: those exhibiting clumpy dust distributions, with sizes and SFR densities typical of sub-mm-selected DSFGs, and those with no evidence of clumpy features and characterized by compact ($R_{eff} < 1$ kpc) sizes and high star formation densities. The latter category is believed to indicate a phase of dissipative contraction before becoming a compact spheroid, and describes both the QSO hosts presented in this paper and the DSFGs presented by Spilker et al. (2020a). The optical/IR sizes of QSO hosts at $z \sim 1.5$ (Silverman et al. 2019), place them between main-sequence and quiescent galaxies, while Ikarashi et al. (2015) found in their sample of $z \sim 1$–3 QSOs and starbursts, that composite sources harbor the smallest sub-mm dust sizes. While all three of our QSO sources lie within the range of dust continuum sizes of the DSFG comparison sample, they do lie at the extreme end of the surface brightnesses. In particular, J2310+1855 exhibits a much smaller continuum size for its IR luminosity and the highest surface brightness of the two samples, possibly indicating that this source is in a more advanced stage in the transformation into a quiescent spheroidal, consistent with the shorter depletion timescale estimated for this source. We note again that our size estimate of P036+03 was significantly larger than previous measurements (Venemans et al. 2020), which would instead make P036+03 our most compact source, and possibly

also further along in its dissipative collapse. This may also provide an explanation for the absence of OH 119 μm absorption in P036+03, as outflows from a more-evolved system may have traveled farther away from the bright central region, and a more compact background emission decreases the total area in which an outflow may be observed. The combination of these effects would decrease the likelihood of an outflowing component intercepting the LOS with the background continuum.

5.4. OH 119 μm Emission

OH 119 μm emission has been detected in many of the low-z galaxy samples (Sturm et al. 2011; Spoon et al. 2013; Veilleux et al. 2013; Calderón et al. 2016; Stone et al. 2016), and is typically associated with the presence of an AGN. AGN fraction, and not simply AGN luminosity, was found to be key in setting the OH 119 μm character (relative strength of emission to absorption) (Veilleux et al. 2013; Stone et al. 2016). In the most AGN-dominated systems where OH is seen purely in emission, Veilleux et al. (2013) notes that the line widths remain modest, possibly indicating a phase after which the galaxy has cleared away the obscuring molecular gas.

Deeper 9.7 μm silicate absorption (a measure of obscuration in both nuclear torii and host galaxy disks) has been found to correlate with fainter OH 119 μm emission and deeper OH 119 μm absorption, indicating that OH 119 μm emission is strongly affected by the geometry of the obscuring material (Stone et al. 2016). While earlier studies argued that OH 119 μm emission originates from the buried nuclear regions of galaxies (e.g., Spoon et al. 2013), where radiative pumping would predominantly excite the OH, Stone et al. (2016) later showed that in some Type 2 AGNs (where the nucleus is obscured), and where the silicate 9.7 μm line is found in absorption, some of the OH 119 μm is still found in emission. Given the apparent impact of obscuring material on OH 119 μm emission this may imply that the OH 119 μm emission also originates farther out than the nucleus, such as in a circumnuclear starburst. Here, physical conditions favor collisional excitation over radiative pumping. Similar conclusions have emerged from a studies measuring the relative strengths of OH transitions (e.g., in NGC 1068; Spinoglio et al. 2005) and in studies using both silicate absorption and multi OH transition data (Runco et al. 2020).

OH 119 μm emission was not detected in any of the Spilker et al. (2020a) high-z DSFGs, consistent with their measured subdominant AGN fractions (all upper limits). OH 119 μm emission is likely present in the $z = 6.13$ QSO ULAS J131911 +095051 (Herrera-Camus et al. 2020), causing the blueshifted absorption observed in it is spectra to exhibit only a single absorption peak, due to superimposed emission and absorption of the low- and high-frequency doublet transitions, respectively. A similar scenario is more clearly observed for P183 +05 in our sample. Tentative emission is also detected for a second of our sources, P036+03, but not in that of J2310 +1855, which instead displays the strongest OH absorption. Thus, as seen at low-z, it appears the presence of an AGN in high-z sources is also required to provide an environment in which OH 119 μm emission may be observed. Also consistent with low-z observations, emission line widths appear to be modest.

All three of our QSOs are unobscured and as mentioned in our previous discussion sections, it is suspected that the

outflowing OH observed in absorption is ejected via star formation feedback and thus likely not to have originated from the nucleus region. It may then be expected that the gas traced by OH 119 μm emission, is also, at least in part, located farther out from the AGN, perhaps in a circumnuclear starburst as predicted for some low-z galaxies (Spinoglio et al. 2005; Spoon et al. 2013; Runco et al. 2020). Furthermore, we find in the case of P183+05, that the OH 119 μm emission is spatially more extended than the background continuum. We cannot however determine with a single OH transition what excitation mechanism is dominant in these sources. Future multiline and spatially resolved OH observations will be needed to elucidate the nature and location of these environments.

6. Conclusion

We present marginally resolved ALMA band 7 observations targeting the OH 119 μm line and dust continuum in three $z > 6$ QSOs: J2310+1855, P183+05, and P036+03. We detect OH absorption for two of the sources (J2310+1855 and P183+05), blueshifted with respect to the host galaxy systemic velocities, and in emission for P183+05 and tentatively P036+03, at systemic velocities. We detail our main results below.

1. We compare the spectral properties of the blueshifted OH 119 μm absorption signatures tracing the molecular outflows in J2310+1855 and P183+05, with those of a comparison high-z DSFG sample (Spilker et al. 2020a, 2020b). We find that the FWHM in both J2310+1855 and P183+05 is narrower than expected for their host galaxy FIR luminosities, but that the EW (absorption strength) of the line is significantly larger in the case of J2310+1855, and comparable in P183+05. This may imply a higher outflow covering fraction or a geometry of the outflow that has a tendency to cover brighter regions of the background dust continuum.

2. Assuming a spherical thin shell geometry, we derive the masses, mass outflow rates, and energetics of the molecular outflows. We find that J2310+1855 and P183+05 have comparable mass outflow rates to the DSFG sample in terms of L_{FIR}. J2310+1855 is significantly offset toward lower energy flux for its L_{FIR}.

3. While the estimated escape fractions of the molecular outflows are negligible, we suggest that energy injected into the CGM via the fast nuclear-driven ionized phase may (Bischetti et al. 2022) may inhibit the re-accretion of this gas back onto the galaxy. This brings our derived depletion times of <1 Myr into agreement with predictions for massive high-z QSOs (Simpson et al. 2012; Costa et al. 2018).

4. We do not find any evidence, nor require any additional input from a central AGN, to drive the observed molecular outflow in J2310+1855 but cannot rule out an AGN contribution for P183+05 if the AGN contribution to L_{FIR} is significant and/or the outflow covering fraction is high (⩾53%), which we find to be an unlikely scenario for our $z > 6$ unobscured QSOs (Venemans et al. 2018, 2020). This suggests that the molecular outflows are driven dominantly by processes associated with star formation, as is expected of the high-z DSFG sample.

5. Consequently, we suggest that the observed spectral differences of the absorption lines are instead caused by differences in the background dust continuum. We demonstrate with an outflow toy model (Figure 7) that for a more compact and/or inclined background dust continuum, observations are limited to fewer outflowing clumps and clumps at low altitudes. This results in narrower absorption line widths (fewer velocity components) and an increase of the projection effects on the outflow velocity, assuming the clumps move in a galactic fountain-like trajectory. For both an increase in inclination, and more compact dust distribution, each individual intervening clump will cover a larger fraction of the overall dust continuum and will have the tendency to cover regions of brighter dust continuum surface brightness. We suggest that J2310+1855's small dust size may make its outflow velocity more sensitive to projection effects, contributing to its slower than expected outflow velocity.

6. J2310+1855's compact dust continuum may indicate that its host galaxy is at a more-evolved stage of dissipative contraction in its transformation into a compact spheroidal (Stacey et al. 2021). The small dust sizes measured in other high-z QSO samples suggest that the effects of the background continuum on the absorption line spectral properties of outflows that we find in this paper, may be a common systematic in future, larger samples.

7. We detect OH 119 μm emission for P183+05, and tentatively for P036+03, in contrast with the high-z DSFG sample where emission is not detected in any of the sources. This is consistent with detections in low-z studies that have found that the presence of an AGN is required to provide the necessary environment to excite the molecules.

Given the limited sample size of three in this study, and the marginally resolved nature of our observations, we note that many of our conclusions are speculative at this time. To determine the geometry and covering fractions of the outflowing molecular gas concretely, spatially resolved observations are crucial. Larger sample sizes will also be required to determine if the differences in outflow spectral properties driven by QSO hosts, as found in this paper, are truly caused by the background dust distribution and not the outflow itself. Similarly, larger samples of DSFGs, particularly at higher ($10^{13} L_{\odot}$) L_{FIR}, are needed to constrain the trends found in the purely star-forming sample, so as to compare between the two possible outflow driving mechanisms better.

Lastly, in this paper we have focused on three unobscured QSOs, sources that have already completed their blowout phase and where energy and momentum injected by the central black hole may efficiently escape the galaxy via the cleared out pathway. Our results suggest that at this evolutionary phase the interaction between QSO and host galaxy ISM is limited. Thus observations targeting QSOs in the lead up to or during the blowout phase may better illuminate the role and impact QSOs play in removing cool gas from their host galaxies.

ORCID iDs

Kirsty M. Butler ● https://orcid.org/0000-0001-7387-0558
Paul P. van der Werf ● https://orcid.org/0000-0001-5434-5942
Matus Rybak ● https://orcid.org/0000-0002-1383-0746
Bram P. Venemans ● https://orcid.org/0000-0001-9024-8322
Fabian Walter ● https://orcid.org/0000-0003-4793-7880
Roberto Decarli ● https://orcid.org/0000-0002-2662-8803

References

Bañados, E., Decarli, R., Walter, F., et al. 2015, ApJL, 805, L8
Bañados, E., Rauch, M., Decarli, R., et al. 2019, ApJ, 885, 59
Berta, S., Young, A. J., Cox, P., et al. 2021, A&A, 646, A122
Bischetti, M., Feruglio, C., D'Odorico, V., et al. 2022, Natur, 605, 244
Bischetti, M., Maiolino, R., Carniani, S., et al. 2019, A&A, 630, A59
Butler, K. M., van der Werf, P. P., Rybak, M., et al. 2021, ApJ, 919, 5
Calderón, D., Bauer, F. E., Veilleux, S., et al. 2016, MNRAS, 460, 3052
Carnall, A. C., Walker, S., McLure, R. J., et al. 2020, MNRAS, 496, 695
Carniani, S., Gallerani, S., Vallini, L., et al. 2019, MNRAS, 489, 3939
Chambers, K. C., Magnier, E. A., Metcalfe, N., et al. 2016, arXiv:1612.05560
Cicone, C., Maiolino, R., Gallerani, S., et al. 2015, A&A, 574, A14
Costa, T., Rosdahl, J., Sijacki, D., & Haehnelt, M. G. 2018, MNRAS, 479, 2079
D'Amato, Q., Gilli, R., Vignali, C., et al. 2020, A&A, 636, A37
Decarli, R., Pensabene, A., Diax-Santos, T., et al. 2022, A&A, 662, A60
Decarli, R., Walter, F., Venemans, B. P., et al. 2018, ApJ, 854, 97
Duras, F., Bongiorno, A., Piconcelli, E., et al. 2017, A&A, 604, A67
Estrada-Carpenter, V., Papovich, C., Momcheva, I., et al. 2020, ApJ, 898, 171
Falgarone, E., Zwaan, M. A., Godard, B., et al. 2017, Natur, 548, 430
Fan, L., Knudsen, K. K., Fogasy, J., & Drouart, G. 2018, ApJL, 856, L5
Feruglio, C., Fiore, F., Carniani, S., et al. 2018, A&A, 619, A39
Feruglio, C., Maiolino, R., Piconcelli, E., et al. 2010, A&A, 518, L155
Fielding, D., Quataert, E., & Martizzi, D. 2018, MNRAS, 481, 3325
Fischer, J., Sturm, E., González-Alfonso, E., et al. 2010, A&A, 518, L41
Fluetsch, A., Maiolino, R., Carniani, S., et al. 2021, MNRAS, 505, 5753
Forrest, B., Marsan, Z. C., Annunziatella, M., et al. 2020, ApJ, 903, 47
Gallerani, S., Ferrara, A., Neri, R., & Maiolino, R. 2014, MNRAS, 445, 2848
Gallerani, S., Pallottini, A., Feruglio, C., et al. 2018, MNRAS, 473, 1909
Ginolfi, M., Jones, G. C., Béthermin, M., et al. 2020, A&A, 633, A90
Glazebrook, K., Schreiber, C., Labbé, I., et al. 2017, Natur, 544, 71
González-Alfonso, E., Fischer, J., Spoon, H. W. W., et al. 2017, ApJ, 836, 11
Governato, F., Brook, C., Mayer, L., et al. 2010, Natur, 463, 203
Guarnieri, P., Maraston, C., Thomas, D., et al. 2019, MNRAS, 483, 3060
Heckman, T. M., & Thompson, T. A. 2017, arXiv:1701.09062
Herrera-Camus, R., Sturm, E., Graciá-Carpio, J., et al. 2020, A&A, 633, L4

Herrera-Camus, R., Förster Schreiber, N., Genzel, R., et al. 2021, A&A, 649, A31
Ikarashi, S., Ivison, R. J., Caputi, K. I., et al. 2015, ApJ, 810, 133
Indriolo, N., Bergin, E. A., Falgarone, E., et al. 2018, ApJ, 865, 127
Jiang, L., McGreer, I. D., Fan, X., et al. 2016, ApJ, 833, 222
Keres, D., Katz, N., Davé, R., Fardal, M., & Weinberg, D. H. 2009, MNRAS, 396, 2332
Khusanova, Y., Bañados, E., Mazzucchelli, C., et al. 2022, A&A, 664, A39
Li, J., Wang, R., Riechers, D., et al. 2020, ApJ, 889, 162
Maiolino, R., Gallerani, S., Neri, R., et al. 2012, MNRAS, 425, L66
Mazzucchelli, C., Bañados, E., Venemans, B. P., et al. 2017, ApJ, 849, 91
McMullin, J. P., Waters, B., Schiebel, D., Young, W., & Golap, K. 2007, in ASP Conf. Ser. 376, Astronomical Data Analysis Software and Systems XVI, ed. R. Shaw, F. Hill, & D. Bell (San Francisco, CA: ASP), 127
Meyer, D. M., & York, D. G. 1987, ApJL, 315, L5
Meyer, R. A., Walter, F., Cicone, C., et al. 2022, ApJ, 927, 152
Neeleman, M., Novak, M., Venemans, B. P., et al. 2021, ApJ, 911, 141
Nguyen, H., Dawson, J. R., Miville-Deschênes, M. A., et al. 2018, ApJ, 862, 49
Novak, M., Venemans, B. P., Walter, F., et al. 2020, ApJ, 904, 131
Pensabene, A., Carniani, S., Perna, M., et al. 2020, A&A, 637, A84
Planck Collaboration, Ade, P. A. R., Aghanim, N., et al. 2016, A&A, 594, A13
Riechers, D. A., Cooray, A., Pérez-Fournon, I., & Neri, R. 2021, ApJ, 913, 141
Rojas-Ruiz, S., Bañados, E., Neeleman, M., et al. 2021, ApJ, 920, 150
Runco, J. N., Malkan, M. A., Fernández-Ontiveros, J. A., Spinoglio, L., & Pereira-Santaella, M. 2020, ApJ, 905, 57
Rupke, D. 2018, Galax, 6, 138
Rupke, D. S., Veilleux, S., & Sanders, D. B. 2005, ApJS, 632, 751
Sanders, D. B., & Mirabel, I. F. 1996, ARA&A, 34, 749
Schneider, R., Bianchi, S., Valiante, R., Risaliti, G., & Salvadori, S. 2015, A&A, 579, A60
Shao, Y., Wang, R., Carilli, C. L., et al. 2019, ApJ, 876, 99
Shao, Y., Wang, R., Weiss, A., et al. 2022, A&A, 668, A121
Sharma, P., Roy, A., Nath, B. B., & Shchekinov, Y. 2014, MNRAS, 443, 3463
Silverman, J. D., Treu, T., Ding, X., et al. 2019, ApJL, 887, L5
Simcoe, R. A., Sargent, W. L. W., & Rauch, M. 2004, ApJ, 606, 92
Simpson, J. M., Smail, I., Swinbank, A. M., et al. 2012, MNRAS, 426, 3201
Somerville, R. S., & Primack, J. R. 1999, MNRAS, 310, 1087
Spilker, J. S., Aravena, M., Béthermin, M., et al. 2018, Sci, 361, 1016
Spilker, J. S., Aravena, M., Phadke, K. A., et al. 2020b, ApJ, 905, 86
Spilker, J. S., Phadke, K. A., Aravena, M., et al. 2020a, ApJ, 905, 85
Spinoglio, L., Malkan, M. A., Smith, H. A., González-Alfonso, E., & Fischer, J. 2005, ApJ, 623, 123
Spoon, H. W. W., Farrah, D., Lebouteiller, V., et al. 2013, ApJ, 775, 127
Stacey, H. R., McKean, J. P., Powell, D. M., et al. 2021, MNRAS, 500, 3667
Stone, M., Veilleux, S., Meléndez, M., et al. 2016, ApJ, 826, 111
Straatman, C. M. S., Labbé, I., Spitler, L. R., et al. 2014, ApJL, 783, L14
Sturm, E., González-Alfonso, E., Veilleux, S., et al. 2011, ApJL, 733, L16
Travascio, A., Zappacosta, L., Cantalupo, S., et al. 2020, A&A, 635, A157
Tripodi, R., Feruglio, C., Fiore, F., et al. 2022, A&A, 665, A107
Valentino, F., Tanaka, M., Davidzon, I., et al. 2020, ApJ, 889, 93
Veilleux, S., Cecil, G., & Bland-Hawthorn, J. 2005, ARA&A, 43, 769
Veilleux, S., Maiolino, R., Bolatto, A. D., & Aalto, S. 2020, A&ARv, 28, 2
Veilleux, S., Meléndez, M., Sturm, E., et al. 2013, ApJ, 776, 27
Venemans, B. P., Bañados, E., Decarli, R., et al. 2015, ApJL, 801, L11
Venemans, B. P., Decarli, R., Walter, F., et al. 2018, ApJ, 866, 159
Venemans, B. P., Walter, F., Neeleman, M., et al. 2020, ApJ, 904, 130
Wang, R., Wagg, J., Carilli, C. L., et al. 2013, ApJ, 773, 44

Erratum: "Molecular Outflows in $z > 6$ Unobscured QSO Hosts Driven by Star Formation" (2023, ApJ, 944, 134)

Kirsty M. Butler[1,2] , Paul P. van der Werf[2], Theodoros Topkaras[2], Matus Rybak[2,3] , Bram P. Venemans[2] ,
Fabian Walter[4] , and Roberto Decarli[5]
[1] Institut de Radioastronomie Millimétrique (IRAM), 300 rue de la Piscine, F-38400 Saint-Martin-d'Héres, France; kirstymaybutler@gmail.com
[2] Leiden Observatory, Leiden University, PO Box 9513, 2300 RA Leiden, The Netherlands
[3] THz Sensing Group, Faculty of Electrical Engineering, Mathematics and Computer Science, TU Delft, The Netherlands
[4] Max-Planck Institute for Astronomy, Konigstuhl 17, D-69117 Heidelberg, Germany
[5] INAF—Osservatorio di Astrofisica e Scienza dello Spazio di Bologna, via Gobetti 93/3, I-40129, Bologna, Italy
Received 2023 May 2; published 2023 June 5

1. Equivalent Width and Derived Properties

In this erratum, we correct a mistake in the derivation of OH 119 μm equivalent width in two sources: J2310+1855 and P183+05. Consequently, we also correct the molecular gas outflow mass, mass outflow rate (MOFR), momentum flux, kinetic energy flux, and depletion times as the derivation of these values involves the equivalent width. We provide an updated version of Table 3 from the published article, and of Figures 3, 5, and 6.

We no longer find significantly larger OH 119 μm absorption EWs in our unobscured QSO sources with respect to the high-z DSFGs from the literature Spilker et al. (2020a, 2020b).

Furthermore, the MOFR, momentum flux, and kinetic energy of the molecular outflows in J2310+1855 and P183+05, as traced by the blueshifted OH 119 μm absorption, are now all significantly offset to lower values with respect to the trends with far-infrared (FIR) luminosity seen in high-z DSFGs (Spilker et al. 2020a, 2020b). Even with an assumed 50% contribution to the FIR luminosity from the central active nucleus, both galaxies appear to have suppressed outflow properties. The star formation rate (SFR) exceeds the MOFR in both sources and is therefore the dominant mechanism responsible for depleting the molecular gas reservoir in these systems. The original conclusion of the published article is therefore unchanged and even reinforced.

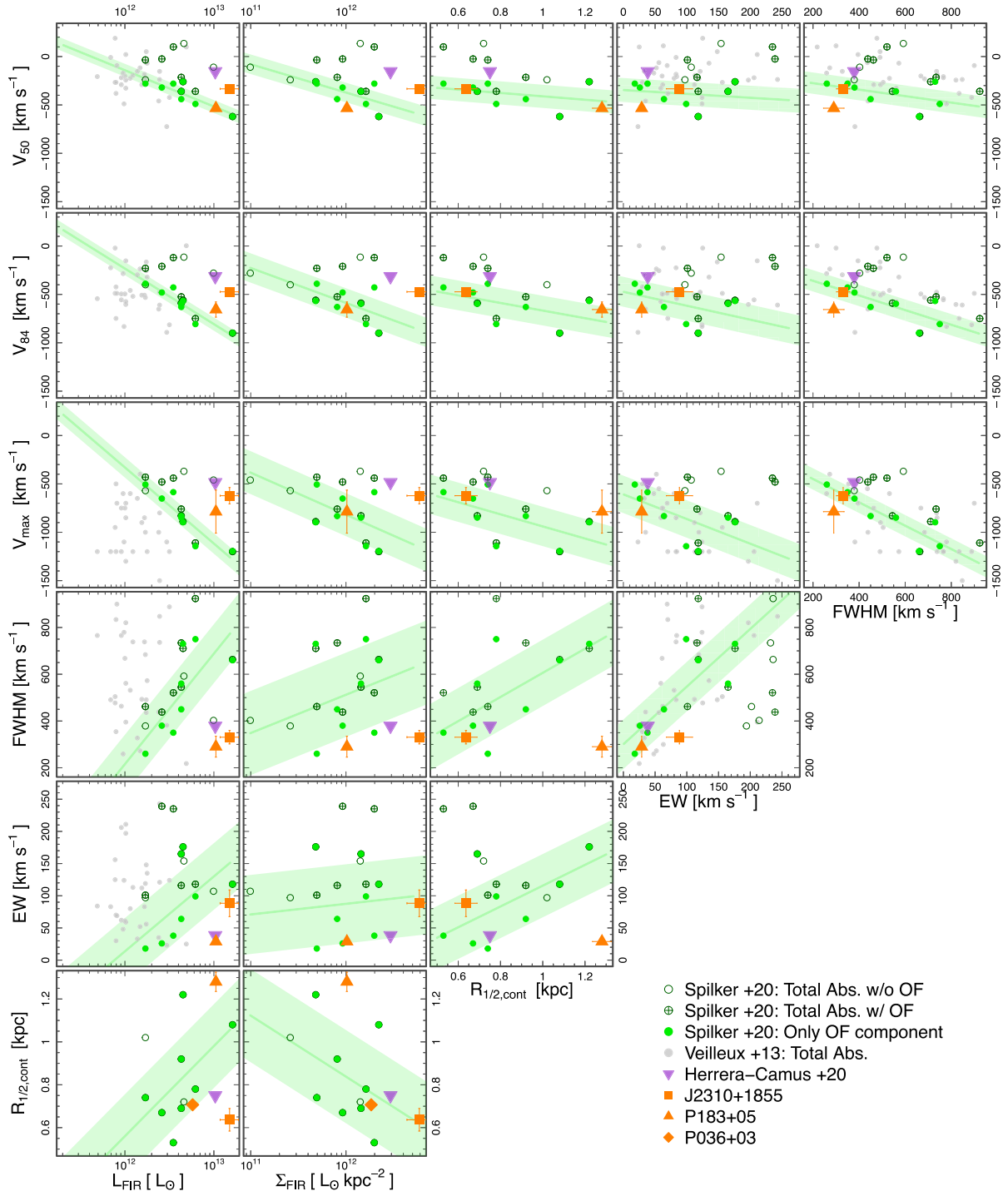We would like to thank Tom Bakx for bringing this error to our attention.

Figure 3. Grid of host galaxy and best-fit OH 119 μm absorption spectra properties. This includes: v_{50}: mean velocity, v_{84}: velocity above which 84% of the absorption lies, v_{max}: velocity above which 98% of the absorption lies, FWHM of the absorption, EW: equivalent width of the absorption, L_{FIR}: FIR luminosity of the host galaxy, Σ_{FIR}: FIR surface brightness of the host galaxy given by $L_{FIR}/(2\pi R_{1/2,cont}^2)$, R_{cont}: effective radius of the 119 μm continuum emission. We show low-z sources in gray, including both star-forming and active galactic nucleus (AGN) host galaxies (Veilleux et al. 2013). The spectral properties are measurements of the total (systemic and blueshifted) absorption lines. In green we show the high-z DSFG sample studied by Spilker et al. (2020a, 2020b), further separating this sample into measurements of the total (systemic and blueshifted) absorption line (dark green crossed circles), just the systemic components (dark green open circles), and just the outflowing components (light green filled). Sources with only an outflowing component will appear as a light green dot with a dark green outline. We display a fit to the outflow—only components in each panel (illustrative only) with a solid line and shade the 1σ scatter, both in light green. We include the tentative OH detection in the $z = 6.13$ QSO, ULAS J131911+095051 (Herrera-Camus et al. 2020; purple triangle). J2310+1855 and P183+05 are shown by the filled orange square and triangle, respectively.
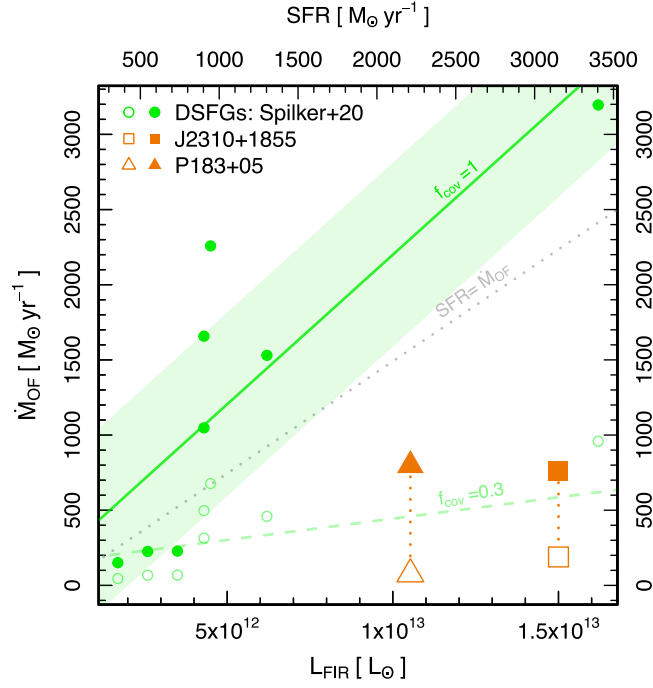
Figure 5. Mass outflow rate as a function of FIR luminosity (bottom axis) and star formation rate (top axis), assuming a spherical thin shell geometry for all sources. We show the DSFGs (Spilker et al. 2020a, 2020b) in green assuming a covering fraction of 1 (filled) as upper limits and 0.3 (hollow) based on the average covering fractions measured for low-z star-forming galaxies (González-Alfonso et al. 2017). We show a fit to the $f_{cov} = 1$ points with the solid green line and its 1σ spread with a shaded green region. A fit to the $f_{cov} = 0.3$ points is shown by the dashed green line. We indicate J2310+1855 and P183+05 with an orange square and triangle, assuming a covering fraction of 1 (filled) as upper limits and at the level of their fractional OH absorption depths, 25% and 9.4% (hollow), respectively. The SFR = $\dot{M}_{OF}$ line is shown by the gray dotted line.

Table 3
Measured and Derived Host Galaxy and Outflow Properties

		J2310+1855	P183+05	P036+03
		119 μm Continuum		
$R_{1/2, 119\ \mu m}$	[pc]	637 ± 53	1280 ± 45	707 ± 22
$S_{119\ \mu m}$	[mJy]	4.73 ± 0.0016	6.66 ± 0.0010	5.00 ± 0.0020
		OH 119 μm Emission (systemic)		
$S_{OH\ 119\ \mu m}$	[Jy km s^{-1}]	$\cdots$	0.28 ± 0.028	0.12 ± 0.022
$\sigma_{Emis.}$	[km s^{-1}]	$\cdots$	123 ± 13	45.9 ± 9.5
FWHM$_{Emis}$	[km s^{-1}]	$\cdots$	289 ± 31	108 ± 22
		OH 119 μm Absorption (outflow)		
$S_{OH\ 119\ \mu m}$	[Jy km s^{-1}]	-0.42 ± 0.04	-0.19 ± 0.03	$\cdots$
$N_{OH\ 119\ \mu m}$	[10^{15} cm^{-2}]	8.90 ± 2.1	3.10 ± 0.059	$\cdots$
EW$_{OF}$	[km s^{-1}]	88.4 ± 21	28.9 ± 0.55	$\cdots$
σ_{OF}	[km s^{-1}]	140 ± 12	123 ± 19	$\cdots$
FWHM$_{OF}$	[km s^{-1}]	330 ± 29	290 ± 45	$\cdots$
V_{50}	[km s^{-1}]	-334 ± 14	-534 ± 18	$\cdots$
V_{84}	[km s^{-1}]	-473 ± 21	-656 ± 79	$\cdots$
V_{max}	[km s^{-1}]	-622 ± 85	-787 ± 222	$\cdots$
M_{OF}	[$10^8\ M_\odot$]	$3.5-14$	$1.8-19$	$\cdots$
$\dot{M}_{OF}$	[$M_\odot$ yr^{-1}]	$190-760$	$75-800$	$\cdots$
$\dot{p}_{OF}$	[10^{35} dyne]	$4.0-16$	$2.5-26$	$\cdots$
$\dot{E}_{OF}$	[10^{42} erg s^{-1}]	$6.6-26$	$6.7-72$	$\cdots$
τ_{OF}	[Myr]	$58-230$	$63-670$	$\cdots$
τ_{OF+SFR}	[Myr]	$10-11$	$17-22$	23

Note. Measured properties of the 119 μm dust continuum (size and flux), OH emission and absorption lines (with formal uncertainties from the fitting procedure), and derived properties of the molecular outflows.
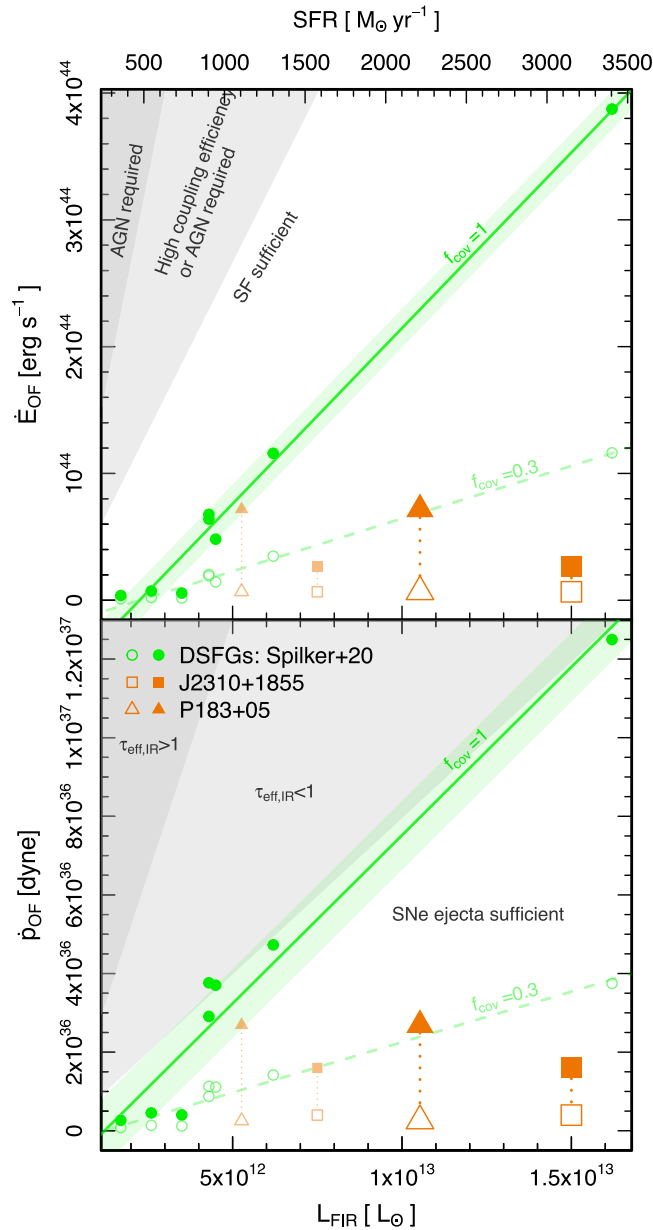
Figure 6. Energy (top) and momentum (bottom) flux as a function of L_{FIR} (bottom axis) and SFR (top axis) derived for the comparison sample of high-z DSFGs (Spilker et al. 2020a, 2020b) (green) and J2310+1855 and P183+05 (orange squares and triangles, respectively). Filled symbols indicate upper limits, assuming an outflow covering fraction of 1. Hollow symbols indicate lower limits for J2310+1855 and P183+05, assuming a covering fraction equal to the fractional OH absorption depth (25% and 9.4%, respectively), and values derived assuming an average covering fraction of 0.3 (González-Alfonso et al. 2017), for the DSFG sample. The smaller faint orange symbols indicate ranges for J2310+1855 and P183+05 assuming a 50% AGN contribution to L_{FIR} (see the main text). We indicate regions in the top panel where the energy injected via star formation, assuming a maximum coupling fraction to the interstellar medium of 40% (Sharma et al. 2014; Fielding et al. 2018), is equal to the energy flux of the outflow (white), where an unusually high coupling fraction or AGN contribution is required (light gray), and where an AGN is definitely required (darker gray). We indicate regions in the bottom panel where supernova ejecta provide sufficient momentum (white) and where radiation pressure on dust grains in an optically thin (light gray) or thick (darker gray) outflow is needed.

ORCID iDs

Kirsty M. Butler https://orcid.org/0000-0001-7387-0558
Matus Rybak https://orcid.org/0000-0002-1383-0746
Bram P. Venemans https://orcid.org/0000-0001-9024-8322

Fabian Walter https://orcid.org/0000-0003-4793-7880
Roberto Decarli https://orcid.org/0000-0002-2662-8803

References

Fielding, D., Quataert, E., & Martizzi, D. 2018, MNRAS, 481, 3325
González-Alfonso, E., Fischer, J., Spoon, H. W. W., et al. 2017, ApJ, 836, 11
Herrera-Camus, R., Sturm, E., Graciá-Carpio, J., et al. 2020, A&A, 633, L4

Sharma, P., Roy, A., Nath, B. B., & Shchekinov, Y. 2014, MNRAS, 443, 3463
Spilker, J. S., Aravena, M., Phadke, K. A., et al. 2020a, ApJ, 905, 86
Spilker, J. S., Phadke, K. A., Aravena, M., et al. 2020b, ApJ, 905, 85
Veilleux, S., Meléndez, M., Sturm, E., et al. 2013, ApJ, 776, 27